Universitetet
i Stavanger

Faculty of Science and Technology

MASTER'S THESIS

Study program/Specialization:	Spring semester, 2024
Structural and Mechanical Engineering / Structural Engineering	Open or ~~Confidential~~

Author: Erling Byberg

Faculty supervisor: Associate Professor Yanyan Sha

Thesis title: Dropped Object Impact Analysis of Subsea Pipelines

Credits (ECTS): 30

Key words:	Number of pages: 66
Non-linear finite element analysis	+ appendix: 3
Subsea pipelines	
Dropped object	
Impact loads	Stavanger 15. June 2024
Plasticity	

MASTER'S THESIS

Dropped Object Impact Analysis of Subsea Pipelines

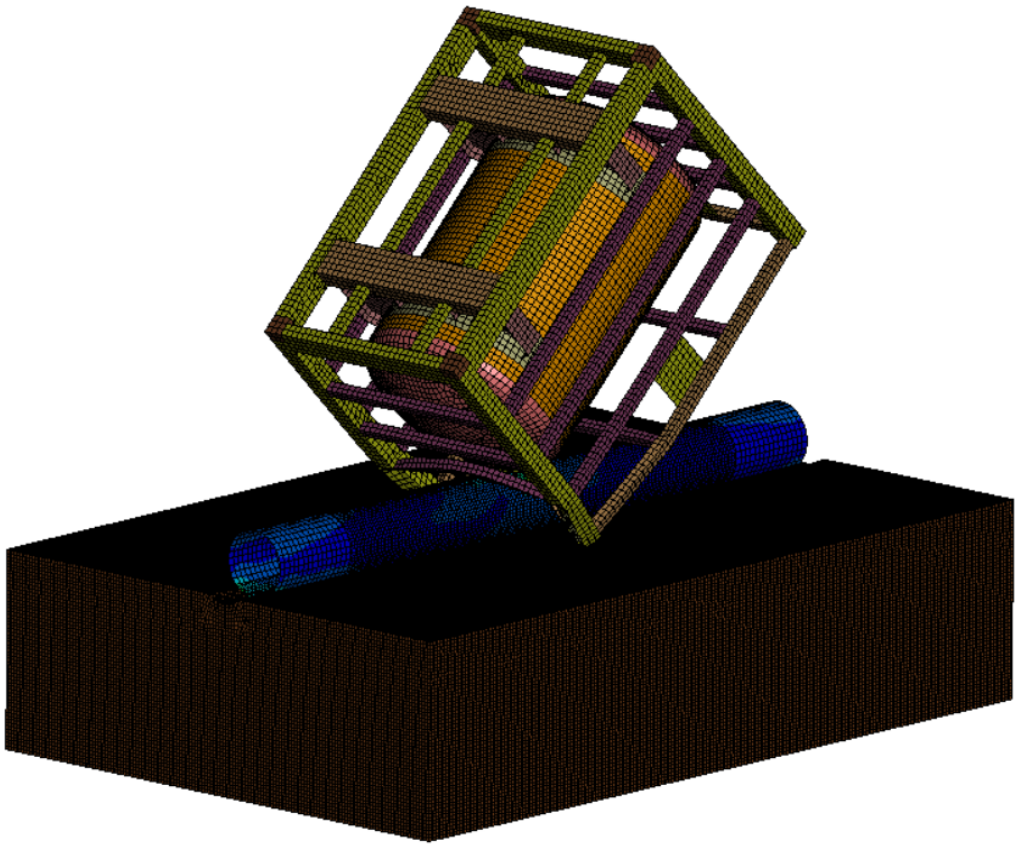

University of Stavanger

Det teknisk-naturvitenskapelig fakultet
Institutt for maskin, bygg og materialteknologi

Preface

This thesis is the final work of the Structural Engineering program at the University of Stavanger. It represents the final step of my academic journey and is a result of the knowledge and experiences I have acquired as a student. The writing process has been both challenging and rewarding, and I am grateful for the support and guidance of those around me, which has enabled me to navigate the work of the thesis successfully.

Firstly, I would like to thank Prof. Yanyan Sha for his guidance, support, and encouragement throughout the writing process. He has given me a good direction on approaching the challenges throughout the thesis, and his experience has been invaluable both in the simulation and writing process. Furthermore, I would like to express my gratitude for the support from IKM Ocean Design, which has provided me with data and information used in this thesis and I am thankful for the office space provided by the company. The simulations in this study were performed on the resources provided by Sigma2 - the National Infrastructure for High-Performance Computing and Data Storage in Norway (project number NN9721K). This support is gratefully acknowledged.

I am also thankful to the Department of Mechanical and Structural Engineering for facilitating an excellent learning environment and offering engaging and interesting structural engineering courses during my studies. And finally, I would also thank my family and friends for being supportive and encouraging during my education.

Stavanger, June 2024

Erling Byberg

.....

Erling Byberg

Summary

This thesis investigates the structural behavior of an impact between a subsea pipeline and a tank with a handling frame. The primary focus has been on comparing the different thicknesses of the pipeline wall and different types of soil. Additionally, the results have been compared with practices given in design codes and methods proposed by other researchers to evaluate how the simulations align with previously established models.

The approach for performing the simulations has been to use numerical analysis with the explicit and implicit nonlinear finite element software LS-DYNA. A total of 11 simulations were carried out to capture the differences in the pipeline's structural response due to different properties for the seabed and pipeline configurations. Pipelines with nominal diameters of 50.0 mm, 25.4 mm, and 12.7 mm were assessed. For the soil types, natural sand and clay have been chosen for evaluation and additionally, three simulations with a rigid seabed were carried out. In all cases, the nominal pipeline diameter has been 20 inches, which corresponds to 508mm.

The loading case has been the same for all simulations. A tank with a handling frame of mass 7550 kg with an initial velocity of 6.3 m/s was utilized. This is equivalent to an impact energy of 149.8 kJ. In the simulations with natural sand and clay, the tank has been deformable. In the simulations with a rigid seabed, the tank has also been rigid. Two different tank position arrangements have been executed. The dimensions of the tank were $2.95 \times 1.85 \times 2.3$ meters.

The results from the rigid seabed simulations have revealed information about the impact capacity of the pipelines, and the observations have been compared to data from DNV, which indicate a good correlation to each other. The observations have also been compared to a deformation profile model proposed by T. Wierzbicki and M. S. Suh, and the model aligned well with the simulations, especially for the pipeline with a 50.0 mm wall thickness. The maximum dent depths obtained were 186.4 mm, 84.2 mm, and 25.2 mm for the 12.7 mm, 25.4 mm, and 50.0 mm wall thicknesses, respectively.

In the simulations with natural sand and clay, a significant amount of energy has been dissipated into the soil and tank, resulting in small and negligible pipeline deformation. The vertical soil displacement was largest for the clay and with an edge impact of the tank. In this case, the vertical displacement was estimated to be 140 mm. In terms of internal energy of the tank, the most critical case was obtained for the soil type natural sand with an edge impact.

In total, the work performed in this thesis has resulted in several findings and results that are relevant for pipeline engineering. However, notable simplifications have been made, so the usability of the results on their own is limited. In addition, the alignment of the results to the models and methods validates the results and makes the findings of the thesis reliable.

Sammendrag

Denne avhandlingen undersøker den konstruksjonsmessige oppførselen til et sammenstøt mellom en undervanns rørledning og en tank med en tilhørende håndteringsramme. Det primære fokuset har vært å sammenligne forskjellige rørveggtykkelser og grunnforhold. I tilegg har resultatene blitt sammenlignet med prosedyrer gitt i standarder og metoder utarbeidet av forskere for å undersøke hvordan simuleringene sammenstemmer med allerede etablerte modeller.

Tilnærmingen for å utføre simuleringene har vært å bruke numerisk analyse med den ikke-lineære "finite element" programvaren LS-DYNA. Totalt ble 11 simuleringer utført for å fange opp forskjellene i rørets konstruksjonsmessige respons på grunn av ulike egenskaper for havbunnen og rørkonfigurasjoner. Rør med nominelle diametre på 50,0 mm, 25,4 mm og 12,7 mm ble analysert. Når det gjelder grunnforhold, ble naturlig sand og leire valgt for evaluering, og i tillegg ble tre simuleringer med en fast havbunn utført. I alle tilfeller har den nominelle rørdiameteren vært 20 tommer, noe som tilsvarer 508 mm.

Lastpåførselen har vært den samme i alle simuleringene. En tank med en håndteringsramme med masse 7550 kg og med en starthastighet på 6,3 m/s har blitt brukt. Dette tilsvarer en sammenstøtenergi på 149,8 kJ. I simuleringene med naturlig sand og leire har tanken vært deformerbar. I simuleringene med en fast havbunn har tanken vært ikke-deformerbar. To forskjellige tankposisjoner har blitt analysert. Dimensjonene på tanken var 2,95×1,85×2,3 meter.

Resultatene fra simuleringene med fast havbunn har gitt informasjon om rørenes sammenstøtskapasitet, og observasjonene er sammenlignet med data fra DNV som indikerer en god korrelasjon med hverandre. Observasjonene har også blitt sammenlignet med en deformasjonsprofilmodell utarbeidet av T. Wierzbicki og M. S. Suh, og modellen sammenstemte godt med simuleringene, spesielt for røret med en veggtykkelse på 50,0 mm. De maksimale oppnådde bulkdybdene var 186,4 mm, 84,2 mm og 25,2 mm for veggtykkelsene på henholdsvis 12,7 mm, 25,4 mm og 50,0 mm.

I simuleringene med naturlig sand og leire har en betydelig mengde energi blitt absorbert av havbunnen og tanken, noe som resulterte i liten og ubetydelig rørdeformasjon. Den vertikale deformasjonen av havbunnen var størst for leiren og hvor tanken treffer med kanten. I dette tilfellet ble den vertikale deformasjonen estimert til 140 mm. Med hensyn til den indre energien til tanken, ble det mest kritiske tilfellet oppnådd for jordtypen naturlig sand med et kant sammenstøt.

Totalt sett har arbeidet utført i denne avhandlingen resultert i flere funn og resultater som er relevante for ingeniørarbeid innen rørledningsfeltet. Imidlertid er det gjort betydelige forenklinger, slik at bruken av resultatene i seg selv er begrenset. I tillegg gjør samsvarelsen av resultatene til modeller og metoder at resultatene er validerte og gjør funnene i avhandlingen pålitelige.

Contents

List of Figures

List of Tables

Abbreviations

FEA	Finite Element Analysis.
FE	Finite Element.
NLFEA	Non-linear Finite Element Analysis.
DNV	Det Norske Veritas.
ALS	Accidental Limit State.
DOF	Degree of Freedom.
NCS	Norwegian Continental Shelf.
GRP	Glass Reinforced Plastic.

1 Introduction

In the perspective of energy consumption, oil and gas are two of the leading contributors to meet the world's continuously increasing demand. As gas and petroleum liquids are natural resources, it is often a considerable distance between the production cite and the location of where the energy is needed. To ensure a universal and reliable energy access, it is necessary with a infrastructure system for transporting the energy to the customers. In addition to large tankers, pipelines are one of the most widely used methods. Because oil and gas are in the liquid and gas phases, they are well suited for transport in such types of systems. Other types of application of subsea pipelines may include transport of clean hydrogen or transport of CO_2 into empty reservoirs for storage.

At the Norwegian Continental Shelf the production takes place offshore and pipelines are installed at the sea bottom. In design of such types of pipelines, there are a lot of considerations to take into account. The loading condition is complex, particularly due to a hydrostatic pressure from the surrounding water and an internal pressure from the flowing fluids and gases. In addition to the constant loadings, accidental events such as dropped object impact must also be evaluated, as this is one of the possible loads that the pipelines can be exposed to.

At offshore production facilities, there are a considerable amount of activities that can result in dropping objects. Even though the occurrence of dropping objects from crane activity are not happening frequently, it is one of the most likely accidental scenarios, and have to be taken into account when designing subsea pipelines for accidental limit state. Operations when loading and unloading supply vessels, result in many repetitive tasks, where there is a possibility of objects hitting the sea and go further into pipelines or other installations on the sea bottom. Some of the reasons can be insufficient hooking of lifted equipment such as containers and drilling equipment, or because of failure of the crane wire.

The consequences of a dropping object can be massive, because of both downtime of the pipeline and biological issues. In a worst case scenario, there may be oil or gas leakage into the sea. Subsea pipelines are placed in areas with a large biological diversity, and waves and currents can move the leakage over large distances and affect the biological life in a corresponding large area. Other types of consequences may be reputation loss and economical losses for involved companies in addition to initaially unexpected repair work.

In the past few years, there have been several large projects of development of new pipelines. At the NCS, one of the main projects has been the completion of oil and gas pipelines from the Johan Sverdrup field to the Mongstad refinery. With a total of 218 km, it is the largest pipeline in the North Sea. On a global basis, there have also been in recent years some accidents of dropping object impacts. According to the Norwegian Ocean Industry Authority, there have also been some drop object accidents at NCS in the past few years, and this will be discussed in further detail in the thesis.

1.1 Objective

The objective of the thesis is to investigate the structural behavior and integrity of subsea pipelines subjected to impact loads from dropping objects. Finding relations between the dent depth and parameters such as impacted energy and wall thickness is of great importance. Another ojective that is of interest is to evaluate the effect of the soil type to the pipeline

behavior and also to find the distribution of dissipated energy in the object, pipeline, and soil. To achieve that, one aim is to create the numerical model as realistic as possible.

Due to a wide range of possible dropping objects, both the impact angle and weight can vary significantly. One of the objectives of this thesis is to investigate how these parameters affect the behavior of the pipeline. Although dropping objects occurs infrequently, its possible consequences make it valuable to investigate and get experience from.

1.2 Methodology

To achieve the objectives of the thesis, several numerical simulations will be performed. The simulations will be carried out with the aid of a finite element software with the capability of handling nonlinearities. To understand the physical concepts behind the indentation of pipelines and impact loads a level of knowledge in plasticity and related fields are required. Therefore, the work of the thesis will also cover principles in plastic behavior of materials in addition to theory about non-linear finite element analysis.

From the simulations, data will be collected and used for analysis and interpretation. After analyzing the data, conclusions will be drawn by comparing the different impact scenarios. The data obtained will also be compared to empirical equations and methods formulated by researchers and design guidelines. Comparing the results is a fundamental aspect of assessing the structural behavior, and this methodology is used throughout the thesis.

1.3 Thesis Structure

Firstly, the thesis will present a literature review and present the work that has been done by other researchers within the field of offshore dropping objects. This includes a review of journal papers, Ph.D. theses, design codes, and guidelines. Furthermore, the relevant theory that is used and applied in the simulations will be presented. This includes both plasticity and non-linear finite element analysis. Theory related to calculation of the terminal velocity, impact energy, energy dissipation and related topics will also be covered.

Moreover, the geometry modeling setup, such as dimensions of the pipeline, dropping object and mesh configuration will be presented. Material properties and the material models for the soil and steel are then presented. Analysis setup with the keyword used and other relevant parameters is also provided.

Then the results of the simulations and the relevant findings will be presented. This includes diagrams showing stress, force, and impact energy to highlight some. In addition, the results from the simulations are compared to each other to more clearly see the differences in the analyzed cases. In addition, contour plots showing displacement and stress values are provided. Finally, the results and simulations are discussed to draw conclusions of the work performed in this thesis.

2 Literature Review

Offshore pipelines as an infrastructure system for gas and fluids have been used for several decades. As a consequence several studies and investigations have have been carried out in the subject of impact loads. In this chapter, some of this research will be presented and discussed as a brief overview with the most important findings and aspects. The research found relevant is a combination of papers, design codes, and investigation reports. The findings of the literature review could give a direction and influence the upcoming work for this thesis. The literature review could also reveal research gaps that might be relevant to study further.

2.1 Design Codes and Guidelines

Several of the DNVs guidelines and recommended practices are discussing the topic of impact loads on subsea pipelines. In addition to the codes from DNV, NORSOK codes are also commonly used in offshore pipeline engineering. These codes are not mandatory to use for the companies. However, in many situations, it is a requirement from the customer, government, or stated in the contract that the pipeline projects should be in compliance with the design codes. For this reason, it is advantageous to have an understanding of what design codes and recommendations mention about pipeline design, fabrication, maintenance, repair work and related fields.

The *DNV-ST-F101 Submarine Pipelines Systems* [17] is a general design code applicable for submarine pipelines. It is a comprehensive overview of design, safety concepts, corrosion protection, and documentation. Additionallly, it covers fatigue calculation of pipelines, non-destructive test methods, and accidental limit state loadings. For loads within ALS, the code is classifying a load as accidental when the probability of occurance is less than 10^{-2}. Regarding dropped object impacts and the corresponding risk assessment, the code is referring to DNV-RP-F107 for further details.

The recommended practice *DNV-RP-F107 Risk assessment of pipeline protection* [16] is a special purpose guideline applicable for evaluating the risk of accidental loadings on risers, umbilicals and pipelines. In addition to the risk associated with dropped objects, the recommended practice is also assessing other accidental events. Examples are impact of installations due to subsea operations, impact due to anchor handling and pull-over or hooking due to trawling activities. To evaluate the risk, the DNV guideline recommends using a methodology with a risk matrix. The columns and rows represent the frequency and the consequences and are given as numbers from 1 to 5. For the frequency, 1 indicates a low probability of occurrence and 5 is indicating a high probability of occurrence. Similarly for the consequence, 1 represents low consequences and 5 is representing high consequences. Based on this, the columns and row results in a matrix where the cells are divided into Acceptable, As Low As Reasonably Practicable (ALARP), and not acceptable regions. The matrix can be used for evaluating whether an event is acceptable or not acceptable, and if the event is between these two regions, the ALARP methodology is used. By using the ALARP design philosophy, the pipelines are designed by taking into account the cost, and an optimal cost-benefit approach is used.

A significant part of the *DNV-RP-F107* code is discussing the probability of different dropping scenarios due to crane operations. Based on lifting data in the period from 1980 to 1986, frequencies are provided for lifting operations with the platform crane and with the lifting system in the drilling derrick. Based on the number of incidents and the number of lifts during

the period, the drop probability was estimated to be $2.2 \cdot 10^{-5}$ for a single lift. It is clear that frequency increases with increasing weight and for lifts greater than 20 tonnes, the drop probability is found to be $3.0 \cdot 10^{-5}$ for a single lift. The code also addresses that these numbers are combined for many different cranes and then are only applicable for general cases. It is also mentioned that it would be a better choice to use data from the respective crane that is used if such information and statistics exist.

Further, the *DNV RP-F107* is discussing classification of pipeline damage and the damage of a pipeline is classified into three different categories. Minor damage (D1), Moderate damage (D2), and Major damage (D3). It is mentioned that for damage in class D1, it is not required to do repair work and there will be no leakage from the pipeline. For a pipeline to be classified into D1, the damage have to be very small, and only small dents in the steel pipeline wall are allowed in this category. However, it is required to do inspections in order to evaluate and assess the structural integrity. Moderate damage implies that the damage is above 5 percent of the pipeline diameter. For this amount of indentation, it is usually required to repair, but there is no leakage from the pipeline. On the other hand, if it turns out to be leakage, the damage is classified into Major damage (D3). For Major damage there are several subcategories, depending on the amount of hydrocarbons released. If there is no leakage the damage is classified as R0 and when there is a release, but with a limited volume it is classified as R1. If there is a large hole or fracture and the total volume is released, it is classified as a R3 damage. The importance of these leakage and damage categories is related to the process of assessing the risk in both an economical and a human safety perspective.

The *DNV RP-F107* is also discussing different protection types for subsea pipelines. This includes concrete coating, polymer coating, and gravel dump to mention the most widely used methods. Polymer coatings have an energy absorption capability in the range between 0 kJ and 10 kJ and compared to other applicable protection methods, the absorption potential is relatively small. For concrete coatings there are specified several equations that can be used to estimate the energy absorption, and in general an absorption capacity of 40 kJ can be used for a 45 mm normal density concrete coating. Other types of protection systems are pipe-in-pipe, concrete blankets, and sand bags. For these types, the energy absorption capability is normally less than 20 kJ. It is also mentioned that trenching has a positive, but limited effect as protection because it reduces the likelihood of impact.

The Norwegian offshore standard *NORSOK N-004 Design of Steel Structures* [9] is a standard that provides guidelines and requirements for steel structures within the oil industry. Although it is a Norwegian standard, it is also used in other offshore regions. When it comes to accidental limit state loads (ALS), the code is outlining in section 9.2 that offshore structures shall be designed in two different steps to be in compliance with the *NORSOK N-001 Structural design*. The first step is to calculate the resistance of the structure against the accidental loading itself. If the resistance of the structure is reduced because of damage due to the accidental loading, the remaining structural capacity has to be checked again in step 2.

Additionally, the design code *NORSOK N-004* mentions that it is possible to use an alternative to non-linear finite element analyses to investigate the structural behavior of dropping object impacts. The alternative is to use energy considerations together with elasto-plastic approaches to calculate the resistance and energy dissipation for different types of structural components. This consists of determining the terminal velocity and using a load-deformation relation to obtain the strain dissipation. Furhter the resistance should be calculated and approaches are

provided for some specific cases. When it comes to dropped objects, the code emphasizes that the resistance should be determined and based upon recognized methods for plastic analysis. In addition, documentation showing that the collapse mechanism aligns with the real deformation profile is required to comply with the code.

2.2 Research Papers

In the literature review, several research papers have been found interesting for this thesis. The work has revealed essential information about how the behavior of the seabed influence the energy dissipation and the capacity of different protection methods. In addition, some papers about the motion of objects falling through water and impact energies for different objects are considered as valuable insight.

In the subject of pipeline protection covers, M. A. Tauqeer and M. C. Ong, have written a paper to assess dropped object damage of GRP covers [13]. The main work during their project was to investigate and evaluate the impact absorption capacities of three different types of pipeline GRP covers. The assessed and compared shapes were square, triangular, and semi-circular protection covers. In order to achieve this purpose, the methodology used was to perform finite element analysis for the capacity calculations. An approach for estimating the impact energy for different objects was also demonstrated. As a result of their study, the triangular shaped GRP cover turned out to be the most efficient in terms of impact absorption capacity. Another significant observation was that the impact energy of oil and gas equipment in many cases was higher than the absorption capacity of the GRP covers. The impact energy of small oil and gas equipment was in the order of 28 kJ and above. For dropping objects due to fishing activities, the impact energy was found to be in the range from 3 kJ to 14 kJ and is in the same order as the capacity of the covers they studied. In the paper they also mentioned that for high energy impacts, such as subsea trees with impact energy of approximately 2600 kJ, it is not convenient to design the pipelines for such amount of impact, but rather have higher safety procedures when installation and lifting of similar equipment is being done.

Another paper written by M. Zeinoddini et al. [23] investigated the effect of seabed flexibility. As there is an interaction between the pipeline and soil, the behavior of the seabed is of great interest. To investigate this, the authors have done numerical simulations which have been validated against experimental data and then a parametric study was performed. The pipeline analyzed was subjected to an internal pressure and the seabed was modeled with a elasto-plastic behaviour. As a result of the study, the authors concluded with several relevant findings. The flexibility of the seabed is found essential for the energy dissipation and thus the damage of the pipeline. In comparison of a rigid and a flexible seabed, it was concluded that the rigid seabed results in larger pipeline dents. For the case of comparing pressurized and non-pressurized pipelines, the study concluded that the localized deformation and dent depth are lower for the pressurized ones.

As the combination of variables related to wind, waves and currents are in most cases unpredictable in advance, the trajectory of the falling object can be described as a stochastic process. This is done in a paper by G. Xiang et al. [21]. The paper outlines the large amount of uncertainties of the surrounding moving water, and because of these random parameters the process can only be described in statistical terms. Even for simple geometries it is mentioned that the impact point on the seabed may vary, even when the initial conditions are the same. For more complex geometries, predicting the motion trajectory and the impact point becomes more

challenging. In addition, the paper suggests using Monte Carlo Simulation to obtain the landing point distribution and the random characteristics of the motion. To use the MCS method, the trajectory is mathematically expressed as a function of several variables. Each variable has an associated probability distribution and the the MCS combines the distributions of all variables, and based on this generates a common distribution for the bottom landing point.

In a paper written by Md. Rokan Uddin Kawasar et al. [8] a probabilistic and numerical modeling analysis for subsea pipeline impact was performed. The applied methodology was a quantitative risk assessment, meaning that both the probability and the consequences of the accident are taken into account. In the workflow for performing the QRA, the work was divided into two main areas, where one was about the statistical analysis and another about the structural assessment of the impacted pipeline. The structural assessment was performed for different cases, and correspondingly the likelihood of each of these events was calculated. Further the risk was defined as the sum of the frequency multiplied by the consequence for all possible accidents. Based on this the authors was able to create diagrams for the relationship between indentation and impact energy. The study is also referring to the design code ASME 31.4, which is stating that the limits for when repair work of the indention is required. If the indentation of a pipeline is greater than 6% of nominal diameter, it is necessary to repair it to ensure compliance with the specified design code. For comparison, the DNV-RP-F107 recommends using 5 percent as a limit when repair work is required, as mentioned previously.

In research done by F. Jiang et al. [7] numerous parameters that affect the pipeline response are evaluated. To list a few, internal wall pressure, seabed flexibility, coating thickness, pipeline wall thickness and burial depth were assessed. The investigation was carried out experimentally and a numerical model was established and validated against the dropping tests. In some cases, pipelines may have non-supported segments due to the variety in topography. The pipeline is therefore not always resting on the seabed. The authors found that an increase in free span length results in a smaller normalized dent depth. The reason is that more of the impact energy is dissipated through global vibrations and deformation. Similarly, for a flexible seabed, the authors found that more of the energy is dissipated by global deformation, rather than local deformation. In addition, the paper also discusses the effect of buried depth and how soil properties affect the dent depth. The buried pipeline was found to have more significant protection capabilities than the effect of a flexible seabed.

Y. Sha et al. performed dynamic response analysis and damage assessment for subsea pipelines subjected to dropped object impacts [22]. The paper investigated the effect of concrete cover, impact angle, and pipeline dimensions. Some of the key findings include that the assumption of the indentor being rigid is in many cases conservative as the indentor most probably will deform. In this regard, it is mentioned that the relative strength of the pipeline and indentor is important to consider. In addition, the study concluded that variations in the angle of impact have a large effect on both the impact force and the damage of the indentor and the pipeline. Concrete cover protection was found to give a significant increase in impact resistance and reduced the steel pipeline damage. Additionally, T. Dirdal carried out a master thesis within the field of dropping objects [4]. In the study, simulations of a container dropping on a subsea pipeline were carried out. In his work, a comprehensive parametric study was executed in which parameters such as yield strength, seabed effects, and protection methods were investigated.

2.3 Investigation Reports

At the NCS, the Norwegian Ocean Industry Authority (Havtil) carries out investigations of accidental events and events that could have resulted in accidents. These investigations are published and available to the public. In the context of dropping objects, several reports discuss the reasons for the accident and what can be done to minimize the probability of such an event happening again. Several reports indicate that crane and lifting activity is one of the main causes of dropping objects.

One of the accidents that Havtil has investigated was a riser-dropping object in 2018 [10]. The event happened at Jotun B located at the Jotun field. The operator was at the time Point Resources. No injuries were reported, but people were nearby during the lift and the consequences of personal injuries was high. The weight of the riser was 15.7 tons and with a drop height of approximately 8 meters, the impact energy was reported to be 1,23 MJ. The riser fell during a lifting operation with a failure of the locking mechanism. In the report, it was mentioned that the lifting equipment should have had a double safety system. The lifting operation was done in the work of well plugging and the riser hit the wellhead. This dropping scenario was not a threat to subsea pipelines, but clearly shows that accidents of dropping objects are present at the NCS.

3 Dropped Object Impact

Dropped object impacts are one of the most significant accidents to offshore pipelines [8]. In a research paper by Kawsar et al. it is mentioned that approximately 47 % of pipeline failures are caused by external impact accidents. In the paper, impacts are also identified as the most common failure scenario, followed by corrosion and material-related factors. Figure 3.1 is obtained from the same paper and shows a schematic overview of an dropping object accident.

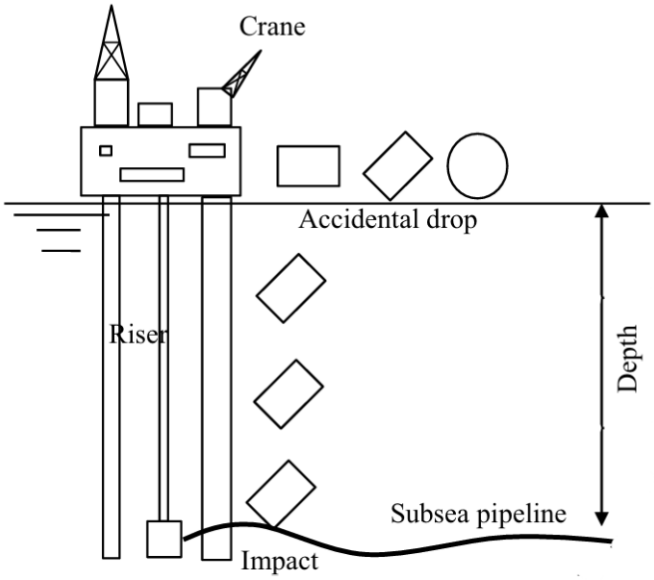

Figure 3.1: Offshore installation and pipeline impact [8]

The accident can be divided into several stages, with the first stage focusing on the cause of the accident. This could be a failure of the crane wire or a similar event, and the position of the object is crucial to determining the object's trajectory. The next phase is the movement of the object through the water, where the object will reach a constant velocity. Lastly, the impact phase occurs when the object hits the pipeline. For large energy impacts, the energy is dissipated into strain energy, and permanent deformations might occur. In Figure 3.2, a pipeline with an indentation is provided to visualize how the deformed shape after an impact might appear. The figure is extracted from one of the simulations performed in the thesis.

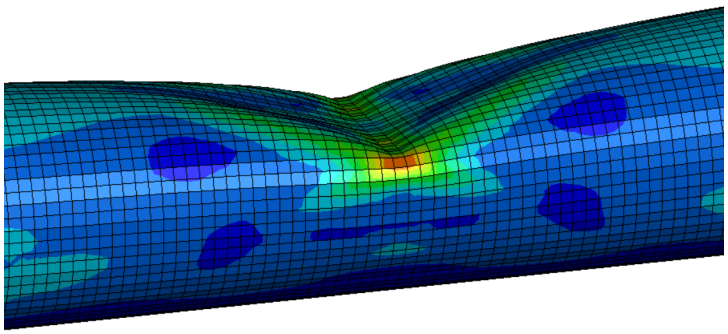

Figure 3.2: Dented pipeline

3.1 Terminal Velocity

When an object hits the water, its velocity will start to accelerate until a threshold value is reached, and then it will continue with constant velocity. The constant velocity of the falling object depends on both the shape and the mass of the object. When the buoyancy force and the drag force equalize the gravitational force of the object, the velocity of the dropping objects becomes constant [16]. This equilibrium condition is used to determine an expression for the constant velocity. The velocity is referred to as the terminal velocity and is given in equation 3.1.

$$v_t = \sqrt{\frac{2g(m - p_w V)}{p_w C_d A_p}} \tag{3.1}$$

In the equation, g corresponds to the gravitational constant of 9.81 m/s^2, m is the mass of the object, p_w is the water density, C_d is the drag coefficient, and A_p is the projected area. The tank used in the simulations has the input values as given in Table 3.1. By substituting these values, the terminal velocity is shown in equation 3.2. In the calculation, it is assumed that the tank contains water with a density of 1000 kg/m^3. It should also be noted that the result is an approximation, due to the uncertainties in determining the dimensions and mass of the tank model.

$$v_t = \sqrt{\frac{2 \cdot 9.81 m/s^2 (7550 kg - 1000 kg/m^3 \cdot 4.8 m^3)}{1000 kg/m^3 \cdot 0.6 \cdot 2.25 m^2}} = 6.3\, m/s \tag{3.2}$$

A comparison of different tank sizes is done to evaluate the effect of the size on the terminal velocity. This is done by assuming an equal shape for all the tanks, and the only varying parameters are the sizes. Offshore tanks normally have a handling frame that induces a large amount of drag forces. In the comparison, the drag coefficient is equal for all cases as the shape is assumed to be the same in all cases. Calculating the drag coefficient accurately requires advanced CFD modeling but for simplification, the drag coefficient is obtained by a research paper about investigation of pipeline protection covers [13]. The coefficient for different tanks in that paper varied around 0.6 and this value was used for the calculation.

Table 3.1: Terminal velocity for different tank sizes

Variable	**Smaller tank**	**Used tank**	**Larger tank**
Tank volume $[m^3]$	2.0	4.8	6.0
Total mass [kg]	3600	7550	9000
Projected area $[m^2]$	2.0	2.25	3.0
Drag coefficient	0.6	0.6	0.6
v_t **[m/s]**	**4.6**	**6.3**	**5.1**

In all of the above three cases, the tanks are assumed to be fully loaded. A full tank is the most critical scenario as the mass increases and hence the terminal velocity increases. It is also possible with an empty tank being dropped, but both the consequences and the likelihood of occurrence are lower, and it is therefore not evaluated here. In the tank comparison table, the

smaller and larger tank values were obtained from IKM. Similarly to the calculation for the tank model used in this thesis, these values are also approximate estimates and may not be entirely accurate.

3.2 Impact and Energy Dissipation

Due to the law of energy conservation, the kinetic energy of the falling object transforms into strain energy in the investigated structure and the object [16]. The kinetic energy associated with the motion of the falling object can be determined by the expression given in Equation 3.3. In the equation, m corresponds to the mass and v_t to the terminal velocity.

$$E_k = \frac{1}{2} m v_t^2 \tag{3.3}$$

To account for added water, the expression for the kinetic energy can be modified as shown in Equation 3.4. The added water mass is introduced to account for the kinetic energy associated with the displaced water, which contributes to the total impact energy.

$$E_k = \frac{1}{2} \left(m + m_a\right) v_t^2 \tag{3.4}$$

The self-weight of the tank was estimated to be 3140 kg and the tank volume was estimated to be $4.48 m^3$. If the tank is assumed to contain water, the total weight is then 7750 kg. Following the same procedure as in the previous section, the terminal velocity for an empty tank is estimated to be 6.3 m/s. By neglecting any contribution from added mass, the impact energy for an empty and full tank is then given in Equation 3.5 and Equation 3.6 respectively.

$$E_k = \frac{1}{2} \cdot (3.140 kg) \cdot (6.3 m/s)^2 = 62,3\, kJ \tag{3.5}$$

$$E_k = \frac{1}{2} \cdot (7.550 kg) \cdot (6.3 m/s)^2 = 149,8\, kJ \tag{3.6}$$

Table 3.2 shows the impact energy for different possible dropping objects from offshore activities and the values are obtained by DROPS [11]. It can be clearly seen that there are large deviations of impact energies for the different dropping objects. As an example, the impact of a subsea tree is 13 times larger than that of a nitrogen tank.

Table 3.2: Impact energy

Object	Mass (kg)	Terminal velocity (m/s)	Impact Energy (kJ)
6” Drill Collar	2.600	6.0	46.8
Nitrogen Tank	12.000	6.0	216.0
5” Drill pipe	1.500	6.0	27.0
Subsea Tree	40.000	12.0	2880.0
Sealed Container	3.500	3.0	15.75
Surge Tank	26.900	8.0	860.8

A relation between impact energy and dissipated strain energy is required to determine the indentation and global deformation of the pipeline. In most real-world cases, this is difficult to

do analytically, but FEA softwares can calculate the force and deformation based on the impact energy. For a system that is not restrained against global motion, the impact could result in movement of the objects in addition to non-recoverable localized deformation. This implies that all the energy not necessary transforms into strain energy.

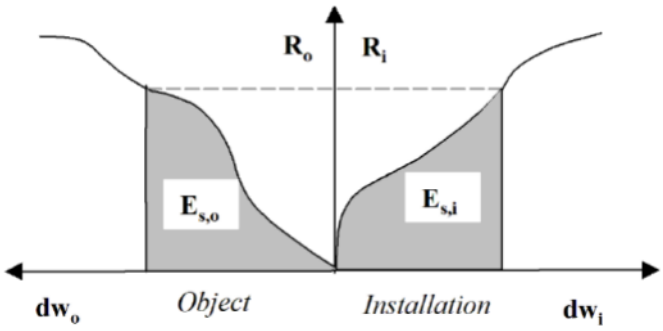

Figure 3.3: Energy dissipation [14]

Figure 3.3 shows a visualization of the energy dissipation of an impact between two different objects. The total dissipated energy is the sum of the dissipated energy of each object and expressed as a function, the strain energy is the sum of the area under the load-deformation curve [14]. In other words, the strain energy is the definite integral of the force with respect to the deformation. This can be seen in Equation 3.7.

$$E_s = E_{s,o} + E_{s,i} = \int_0^w R_o dw_o + \int_0^w R_i dw_i \tag{3.7}$$

The DNV-RP-F107 [16] proposes a relationship between absorbed energy and dent depth for tubular members. The relation is given in Equation 3.8 and shows that the dissipated energy depends on wall thickness (t), plastic moment capacity (m_p), pipeline diameter (D) and indentation (δ). The plastic moment capacity for tubular members is shown in Equation 3.9.

$$E = 16 \left(\frac{2\pi}{9}\right)^{\frac{1}{2}} m_p \left(\frac{D}{t}\right)^{\frac{1}{2}} D \left(\frac{\delta}{D}\right)^{\frac{3}{2}} \tag{3.8}$$

$$m_p = \frac{1}{4}\sigma_y t^2 \tag{3.9}$$

The relation is valid for indentations where the load is applied perpendicularly and as a knife edge and the indentor must cover the whole cross section as shown in Figure 3.4. For a cube or a circular shape, the indentation will differ somewhat and the expression is no longer a good approximation.

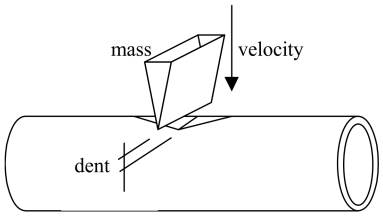

Figure 3.4: Indentation of pipeline [16]

From the ring model, the initial plastification loads for tubular members can be determined. By using the concept of equilibrium of internal and external work, the initial plastification load can be expressed as in Equation 3.10.

$$P_0 = \frac{4m_p}{r} \tag{3.10}$$

By substituting Equation 3.9 into Equation 3.10, it can be seen that by increasing the wall thickness by a factor of 2, the initial plastification load will increase by 4.

$$P_0 = \frac{4}{r} \cdot \frac{1}{4}\sigma_y t^2 = \frac{\sigma_y}{r} t^2 \tag{3.11}$$

3.3 Indentation Models

Wierzbicki and Suh created an indentation model in 1988 [19]. This model makes it possible to calculate the indentation at any point along the pipeline based on the maximum indentation, pipeline diameter, and wall thickness. The indentation at any point along the pipeline is denoted w and is given in Equation 3.12.

$$w = w_d \left(\frac{1 - x}{\xi} \right)^2 \tag{3.12}$$

Where w_d corresponds to the maximum indentation and x is the distance along the pipeline. In the equation, the length of the affected zone is denoted ξ and can be calculated according to Equation 3.13. From the equation, it can be seen that reducing the diameter by 50 % will result in a reduced affected zone of 50 %. Accordingly, by doubling the wall thickness, the affected zone is reduced by 30 %.

$$\xi = \sqrt{\frac{\pi D^2 w_d}{6t}} \tag{3.13}$$

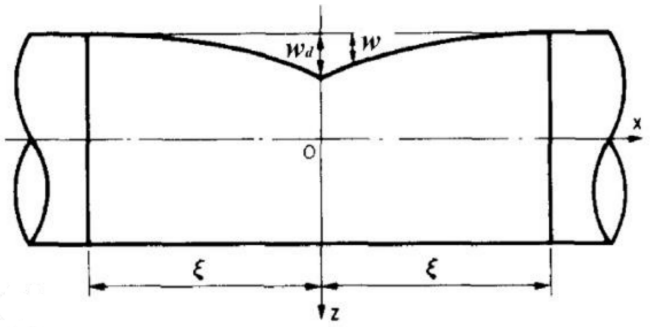

Figure 3.5: Indentation model [19]

4 Plasticity Theory

For loading until the yield strength, there will only be linear elastic strain ε_e. When a material reaches the yield point, the material can be further loaded and beyond this limit, inelastic material behavior occurs and unrecoverable plastic strain ε_p starts to accumulate in the material. To have plastic behavior, the material must be ductile, which is true for most metals and steels. For a simple case of a tensionally uniaxially loaded specimen, plasticity will occur when the specimen is loaded beyond the yield stress of the material.

In the context of impact loads, plasticity plays a significant role because in most cases there will be a certain amount of permanent deformation. In such situations, the material behavior is governed by plasticity. Further in this chapter theory related to plasticity will be presented.

4.1 Strain Hardening

There are different types of strain hardening models available, and some of the most common are isotropic and kinematic hardening models. The characteristic of the isotropic hardening model is that the yield surface expands uniformly in all directions and the effect to the stress-strain curve is shown in Figure 4.1 where the kinematic hardening model is also provided. The material model considered for the steel in this thesis uses an isotropic hardening model, similar to the Figure 4.1 (a).

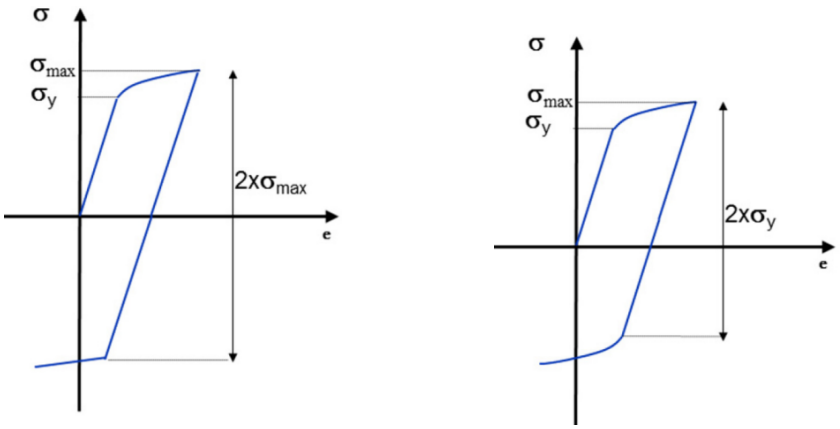

(a) Isotropic hardening *(b) Kinematic hardening*

Figure 4.1: Hardening models [15]

4.2 Yield Criterion

The yield function or yield criterion decides when the material starts to accumulate unrecoverable plastic deformation. As loads in most cases are complex, the stresses at a point in the material usually act in several directions. Because of this, it is not sufficient that the stresses in a given direction are less than the yield stress. Yielding or inelastic material behavior may occur under multiaxial stress, even none of the individual stress components σ_x, σ_y or σ_z exceeds the uniaxial yield stress. To handle this phenomenon, a yield criterion is used to decide whether the applied stress results in yielding or not.

There are several types of yield criteria available for use, where the Von Mises yield criterion is one of the most widely used for modeling steels in structural engineering purposes. For soil materials, yield criteria such as the Mohr-Coulomb criterion are more suited. The criteria can

be represented graphically by yield surface plots and these can be used to decide whether yield has occurred or not. Figure 4.2 shows the Von Mises yield surface in the principal 2D stress space. For a given combination of the two principal stresses σ_1 and σ_2, the yield surface displays if we have yielding or not.

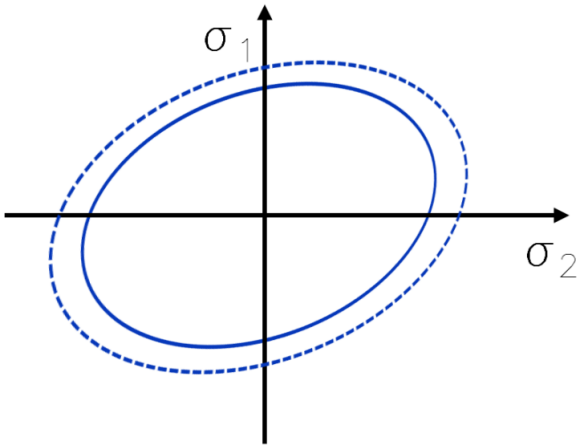

Figure 4.2: Von Mises yield surface [15]

The Von Mises yield criterion combines the stress components into an equivalent or effective stress σ_{eff}. The effective applied stress must be less than the yield stress of the material. In terms of principal stresses, the effective Von Mises stress can be expressed as in Equation 4.1. The equation can also be rewritten in terms of the x, y and z stress components, which is shown in Equation 4.2.

$$\sigma_{eff} = \sqrt{\frac{1}{2}\left[(\sigma_1 - \sigma_2)^2 + (\sigma_2 - \sigma_3)^2 + (\sigma_3 - \sigma_1)^2\right]} \tag{4.1}$$

$$\sigma_{eff} = \sqrt{\frac{1}{2}\left[(\sigma_x - \sigma_y)^2 + (\sigma_y - \sigma_z)^2 + (\sigma_z - \sigma_x)^2\right] + 3\left(\tau_{xy}^2 + \tau_{yz}^2 + \tau_{xz}^2\right)} \tag{4.2}$$

To evaluate if the considered material model PIECEWISE_LINEAR_PLASTICITY is in the plastic regime and yield is reached, a yield function is used. In the material model the yield function is based on the Von Mises yield criterion, and in the software documentation this type of plasticity is called J2 based plasticity, as it is based on the second deviatoric stress invariant, which is often denoted J_2. The formula for the yield function is given in Equation 4.3, where σ_{eq} corresponds to the equivalent Von Mises stress and σ_y is the yield stress. If the strain rate effects are taken into account, the yield stress becomes a function of plastic strain, as there is a possibility of defining different stress-strain curves for different strain rates.

$$\Phi(\sigma) = \sigma_{eq} - \sigma_y(\varepsilon^p) = 0 \tag{4.3}$$

For a negative value of Φ, the material's yield stress is greater than the equivalent stress at a point. In such a case, the material experiences an elastic behavior. When the material's yield stress and the equivalent stress are equal, yielding occurs and a flow rule governs the plastic material behaviour.

$$\Phi(\sigma) \leq 0 : Elastic\,behaviour$$

$$\Phi(\sigma) = 0 : Yielding$$

Both the yield function and the flow rule of the material can be plotted in a principal stress space. For the yield function, the result is a cylinder centered about the hydrostatic axis. A principal stress state that results in a coordinate inside the cylinder refers to elastic material behavior, and similarly a stress state on the cylinder's surface refers to material yielding.

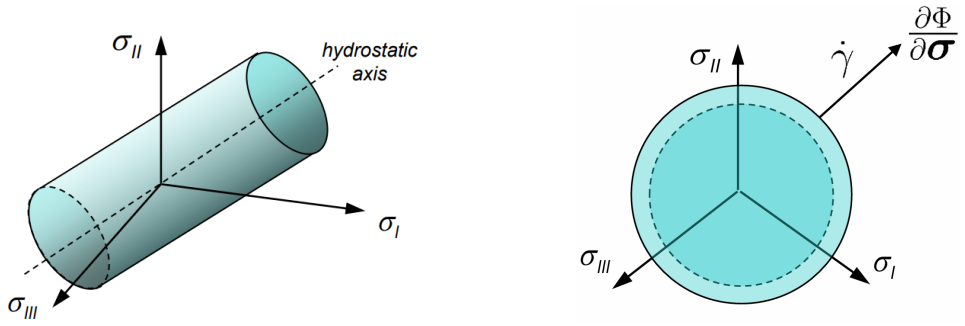

(a) Yield function *(b) Flow rule*

Figure 4.3: Yield function and flow rule in principal stress space [5]

The grapical representation of the flow rule in Figure 4.3 (b) can be described with the Equation 4.4. When plastic deformation has begun, the flow rule governs the material behavior.

$$\dot{\varepsilon}^p = \dot{\gamma}\frac{\partial \Phi}{\partial \sigma} = \frac{3}{2}\dot{\gamma}\frac{S}{\sigma_{eq}} \tag{4.4}$$

4.3 Strain Rate

The rate of deformation or strain rate can have effects on the results in a simulation. The strain rate is the ratio between the change in strain and the change in time, and the formula for the strain rate is shown in Equation 4.5. For dynamic forces with rapid changes, the strain rate may induce additional effects as the high speed of loading has the potential to result in incorrect material response and inaccurate stress and strain predictions.

$$\dot{\varepsilon} = \frac{d\varepsilon}{dt} \tag{4.5}$$

The piecewise linear plasticity material model has the capability of handling strain rate effects, which is relevant for rapid loadings such as impact forces from dropping objects. Several approaches can be used to take into account strain rate effects, and one common method is the cowper-symonds equation. It is a scaling factor that depends on the change in effective strain, $\dot{\varepsilon}^p_{eff}$, and the two parameters C and p. The stress is multiplied by this factor.

$$\sigma_y(\varepsilon^p_{eff}, \dot{\varepsilon}^p_{eff}) = \left[1 + \left(\frac{\dot{\varepsilon}^p_{eff}}{C}\right)^{1/p}\right] \sigma^S_y(\varepsilon^p_{eff}) \tag{4.6}$$

4.4 Plasticity for the Soil Material

Soils behave quite differently from steel and similar materials, and this must be considered in the modeling and simulation. In this regard both the type of discretization and the available material models are relevant to study further. As soils in some cases may be expected to have large deformations, this is also a consideration that requires attention in the modeling.

A frequently used model for soils in LS-DYNA is the SOIL_AND_FOAM material model. The yield function is a deviatoric perfectly plastic yield criterion which implies that the material's yielding behavior is governed by a condition related to the deviatoric stress and when this condition is met, the material undergoes perfectly plastic deformation. The yield function is shown in Equation 4.7.

$$\phi = J_2 - [a_0 + a_1 p + a_2 p^2] \tag{4.7}$$

In the equation, J_2 corresponds to the second deviatoric stress invariant, p is the pressure and a_0 a_1 a_2 are mathematically constants. The deviatoric stress invariant can be expressed in several different ways. The material manual uses the notation given in equation 4.8 and the second deviatoric stress invariant is then given as 0.5 multiplied by the square of each component in the deviatoric stress tensor, s_{ij}.

$$J_2 = \frac{1}{2} s_{ij} s_{ij} \tag{4.8}$$

A characteristic feature of yield functions is how they are affected by a change in pressure. The criteria can either be pressure dependent or pressure independent. In this regard, the stress tensor becomes relevant as it can be divided into a term related to pressure or volume change, also known as the hydrostatic stress, and a term related to shape change, the deviatoric stress. In general, this model is pressure dependent, but there is an option to remove the dependency. In the material model manual it is mentioned that if the constants a_1 and a_2 are set to 0, the yielding is independent of the pressure. This can also be seen in Equation 4.7 where the only remaining terms will be the second deviatoric stress invariant and the a_0 coefficient.

Figure 4.4 shows the behavior of the model in a stress-volumetric strain diagram. For compressive loading, the soil follows the upper line. For unloading, there are to options for material behavior. Volumetric crushing can be turned on or off. By enabling volumetric crushing, the soil's behavior will follow the bottom line and for volumetric crushing turned off, the unloading curve will be the same as the loading curve. Additionally, a pressure cutoff value can be specified in order to determine at which value tensional fracture should occur.

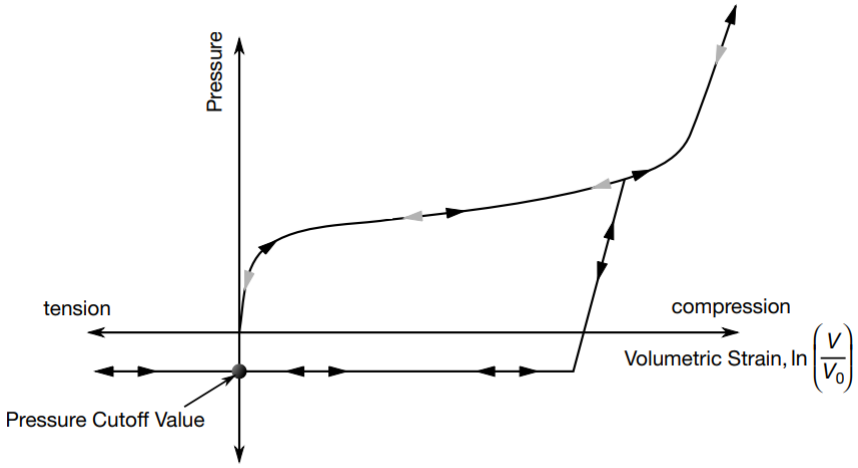

Figure 4.4: Stress strain curve for MAT_005

5 Non-linear Finite Element Analysis

Finite element analysis (FEA) is a numerical method for solving complex engineering problems. It is a technique used in many different disciplines, and some examples of fields that use FEA are structural, electrical, fluid dynamics, and heat transfer. Mathematically, the method is about solving differential equations. As its basic format, the method has limitations as it can only handle problems within the linear range. In most of the real-life problems, non-linearities arise because there typically is not a linear relationship between the variables involved. To go beyond the linear limitation of FEA and extend the feasibility, the non-linear finite element analysis (NLFEA) is implemented.

From a structural engineering point of view, there are three main types of non-linearities. Geometric non-linearity arises in problems with large displacement and cases with higher-order effects such as the P-Δ effect. Material non-linearity is relevant where there is no linear constitutive equation, meaning that there is no linear relationship between the applied stress and corresponding strains. Boundary non-linearity is related to the contact and boundary conditions of the system. Examples that may induce non-linearity are changes in boundary conditions during the simulation and frictional contact.

As FEA and NLFEA both are numerical approaches for solving problems, the user has to be aware of its weaknesses and limitations. By using numerical methods, the results are approximations and compared to analytical solutions there can be relatively large deviations. The accuracy of the solutions are depending on input variables such as type of element used and mesh density and the users ability to turn the physical problem into an, as realistic as possible, FE model.

5.1 Workflow

The workflow in FEA is divided into several stages. These stages typically include pre-processing, analysis setup and post-processing, which are essential for accurate simulation and interpretation of the results. Pre-processing is the part that includes geometry modeling and mesh generation. In addition, the material modeling and assigning the material are parts of the pre-processing phase. Analysis setup includes defining boundary conditions, loading and also to choose the settings for the solver. This could be to choose between implicit and explicit solvers or select the timestep for the solver. In the post-processing stage, results are extracted, and the main goal is to show and interpret the results. This includes tasks such as creating contour plots for different stress types and visualizing deformations.

5.2 Governing Equation

In linear finite element analysis, there is a linear relationship between the applied forces and the resulting displacements. This relationship can be described by the nodal force vector, the stiffness matrix and the displacement vector and is given in equation (5.1). From the equation, it can be seen that the force vector, $\{f\}$, is directly proportional to the displacement vector, $\{U\}$, through the stiffness matrix [K].

$$\{F\} = [K]\{U\} \tag{5.1}$$

On the other hand, NLFEA does not have a linear relationship between the stresses and strains and as the simulation progresses, the geometry of the model changes, meaning that the stiffness matrix changes with displacement taking place. In other words, the stiffness matrix becomes a function of displacements, and this can be seen in equation 5.2.

$$\{F\} = [K(U)]\{U\} \tag{5.2}$$

As the stiffness matrix [K] in NLFEA is a function of displacements, the stiffness matrix changes for each step in the solution. The FEA solver has to do an iterative process, by calculating new solutions for the stiffness matrix based on the obtained stiffness matrix in the previous solution step. Due to this, it requires a higher amount of computational capacity to perform non-linear FEA than linear FEA.

Equation (5.2) does not cover the dynamic effects of the system. A general form of the governing equation, which includes dynamic effects, is given in DNV-RP-C208 [15]. The equation takes into account damping and dynamic forces. The general system of equations for solving any finite element problem is given as in equation (5.3). In the expression, M is the mass matrix, u is the displacement vector, C is the damping matrix, F_{int} is the internal forces and F_{ext} is the external forces.

$$M\ddot{u}(t) + C\dot{u}(t) + F_{int}(t) = F_{ext}(t) \tag{5.3}$$

5.3 Element Formulations

There are three main aspects to consider regarding element formulations: the element's shape, node configuration, and integration points inside each element. To start with the shapes, there are many available shapes, and the most used are solid elements, plate elements, shell elements, bar elements, and spring elements, each with its own advantages and disadvantages depending on the case of use. Within each element, there are a certain number of nodes. The nodes locations and number of nodes in each element are fundamental for the numerical accuracy and computational cost in the simulations. The integration points also have a significant effect to the simulation, as these are the points where the stresses and strains are evaluated.

An element can be fully-integrated or under-integrated and this is related to the number of integration points. The integration points are the specific locations within an element where the function is evaluated during numerical integration. Figure 5.1 (a) shows a plane element with one integration point and Figure 5.1 (b) shows a fully integrated plane element with four integration points, which means that the integration points cover the entire domain of the element.

(a) Reduced integration *(b) Fully integrated*

Figure 5.1: Fully and reduced integration elements [1]

5.3.1 Shell Elements

Shell elements are characterized by a smaller thickness compared to the other dimensions. They are appropriate for modeling thin-walled structures and have the benefit of normally having fewer degrees of freedom than solid elements. Shell elements also have the advantage of modeling both in-plane and out-of-plane deformation. The in-plane deformation is commonly referred to as the membrane effect and considers tension and compression stresses within the plane. Capturing the out-of-plane behavior or bending is beneficial in cases where the elements deform perpendicular to the element's surface. This is achievable due to its out-of-plane DOF, which can be seen in Figure 5.2 (a) and is denoted dz.

As the stresses and strains often vary with the thickness of the shell elements, through-thickness integration of the element ensures that this is accounted for. Through-thickness integration is valuable for structures with a non-uniform thickness as this allows for forces and displacements to be accurately represented between the elements.

In the simulations, the shell elements used were the Belytschko-Tsay elements (ELFORM=2). This is a shell element with one integration point and is the default shell element in the LS-DYNA software. From Figure 5.2 (a), it can be seen that the element has 5 DOF in the local coordinate system, which globally corresponds to 6 DOF as the element can be rotated in terms of global coordinates.

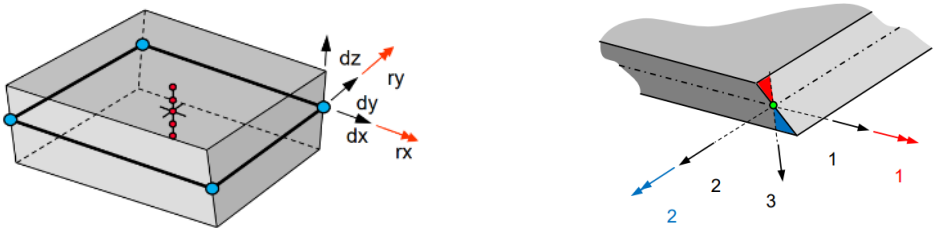

(a) Overview *(b) Shearing*

Figure 5.2: Belytschko-Tsay Shell Element [6]

The behavior within an element is described by the shape functions. For the shell element considered, the shape functions are bi-linear, meaning that the behavior of the element between two nodes can be described by two linear segments. The expressions for the shape functions for the Belytschko-Tsay element are given in equation 5.4 - 5.7. These expressions are also valid for other shell elements with a 4-node configuration. In the equations, ξ and η are used as notations for the axes of the local coordinate system of the element.

$$N_1 = \frac{1}{4}(1-\xi)(1-\eta) \tag{5.4}$$

$$N_2 = \frac{1}{4}(1+\xi)(1-\eta) \tag{5.5}$$

$$N_3 = \frac{1}{4}(1+\xi)(1+\eta) \tag{5.6}$$

$$N_4 = \frac{1}{4}(1-\xi)(1+\eta) \tag{5.7}$$

5.3.2 Solid Elements

In contrast to the shell elements, solid elements are used for geometries with larger thicknesses. In addition to shell elements, solid elements are also used in the simulations. The solid element formulation (ELFORM=1) is known as a constant stress solid element. It is a single-point integration element with 8 nodes. Because of the under-integration, it requires hourglass control to avoid zero-energy modes.

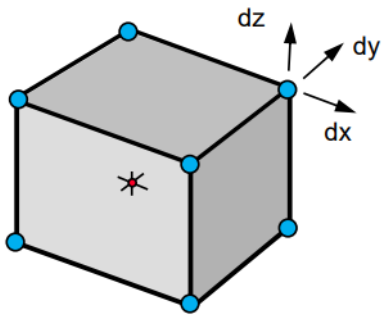

Figure 5.3: Constant Stress Solid Element [12]

5.4 Critical Time Step

In finite element analyses, the critical time step is essential to ensure a stable analysis with reliable results. Solving dynamic non-linear analyses is an iterative time-dependent process where the timestep between each set of equations affects the accuracy. During the computation, the system of equations is evaluated using a time increment equal to the timestep. Consequently, using a large timestep will result in large differences in numerical values for two consecutive calculations of the system of equations. As a result, this may lead to inaccuracy because rapid changes in the system's behaviour are not detected and accounted for. In simulations, the critical timestep is defined as the timestep needed for an appropriate solution. The critical time step is an estimation and it depends on both material properties and mesh dimensions.

In accordance to the LS-DYNA Theory Manual, the time step for shell and solid elements are given as in equations 5.8 and 5.9 respectively. The critical time step is given as the characteristic length of the smallest mesh element over the speed of sound waves in the considered material. In the equations, E is the modulus of elasticity, ρ is specific mass density and ν is Poisson's ratio.

$$\Delta t_{c,shell} = \frac{L}{c} = L\sqrt{\frac{\rho(1-\nu^2)}{E}} \tag{5.8}$$

$$\Delta t_{c,solid} = \frac{L}{c} = L\sqrt{\frac{\rho(1+\nu)(1-2\nu)}{E(1-\nu)}} \tag{5.9}$$

The number of iterations that have to be computed by the solver can be obtained by the ratio of simulation time and the time step. By adjusting these numbers, it is possible to change

the amount of data that has to be processed and correspondingly the computational cost. By assuming a fixed simulation time, the time step is the governing parameter for the number of iterations. To change the time step there are several methods available. Applying a coarser mesh and will result in a increased characteristic length and then the time step will increase. This will result in a faster simulation, but with a lower accuracy.

Another alternative to increase the time step is to mass-scale the elements. This is convenient to do if a small amount of elements have a lower critical time step than others. The smallest elements are then given an additional mass. Since only a small amount of the total number of elements is changed, it will not affect the global accuracy much.

The software used in this thesis automatically calculate the critical time Δt and use it in the simulation. A safety factor of 0.9 is implemented and used by default. Then the time step can be expressed as in equation 5.10.

$$\Delta t = 0.9\Delta t_c \tag{5.10}$$

5.5 Explicit Time Integration

The general equation of motion is a 2^{nd} order differential equation. In the equation, u is the displacement, $\dot{u}$ is the velocity and $\ddot{u}$ is the acceleration. In most engineering problems the displacement are the unknown parameter. Velocity and acceleration are first and second order derivatives of displacement with respect to time, thus finding a expression for the displacement also gives the other two parameters. When solving the general equation of motion, a solution is found for every timestep considered. In the equation, the mass, damping, and stiffness are known parameters and the solution contains the on beforehand unknown displacements. As the method finds solutions over a period of time, the solution process is noted time integration. To handle these time integrations, there are two main options. For static analyses the most convenient method is implicit method and for dynamic analyses with high strain rates, explicit method is the most suitable.

$$[M]\ddot{u}(t) + [C]\dot{u}(t) + [K]u(t) = F(t) \tag{5.11}$$

One of the most important things about time integration, is how the solver determines the value at next timestep and the way of doing this, is the most distinct difference between implicit and explicit solvers. The explicit method uses only the current value, and its derivative to determine the value at next timestep. This is shown in equation 5.12, where the velocity at the next timestep, i.e. n+1, is determined by adding its current value and the timestep multiplied with the derivative at the current timestep. This is in contrast to the implicit method, where the derivative at the next timestep is used and not the derivative of the current. The consequence of this is that explicit requires less computational capacity as the derivative can be found directly, but the accuracy is lower as the correct way is to use the slope at next timestep.

$$u(t_{n+1}) = u(t_n) + \Delta t\dot{u}(t_n) \tag{5.12}$$

In this thesis, the simulation of the dropping object and the pipeline is expected to have high strain rates because of the high speed of the dropping object. The level of non-linearities is

also factor that weighs against using an explicit solver. As a result of those considerations, the explicit solver has been found most appropiate and is used for all simulations.

5.6 Hourglass Control

In FEA analysis, stresses and strains are evaluated at the integration points, and deformations are evaluated at the nodes. This difference can result in issues, as there is a possibility that the deformation of elements is not represented by the strains. Such conditions are called hourglass modes or zero energy modes, as the zero strain values indicate no energy, even though there should be some value for the strain as there is deformation in the element. As Figure 5.4 shows, the element is deformed because of changes in node locations. The integration point is still at the same position, and in this case it is no associated strain values to the displacement.

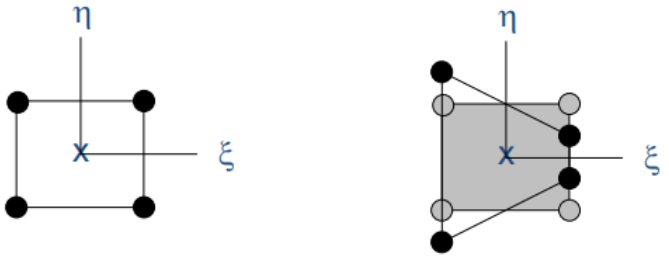

(a) Undeformed element *(b) Hourglass mode*

Figure 5.4: Undeformed quadrilateral element and corresponding hourglass mode [8]

If the hourglass energy is relatively high compared to the system's internal energy, it is required to limit this dissipation of energy by using hourglass control. In the simulations, hourglass control is used to reduce the amount of hourglass energy of the soil. As an alternative to hourglass control, fully integrated elements can be used in order to avoid hourglass energy. For the fully integrated elements, the nodes and integration points are at the same location, and hourglass modes will for this reason not occur. In the simulation a Flanagan-Belytschko stiffness form was used for the hourglass control.

5.7 Discretization

5.7.1 Soil Discretization

The most commonly used methods for discretization of soils are lagrangian, eulerian, arbitrary lagrangian-eulerian methods. All of these methods uses a mesh and the difference between them are how the mesh and the material interacts. As default, the software used in this thesis employs Lagrange discretization. In this method, the material is connected to the mesh. As the material undergoes deformation, the mesh will also deform. On the other hand, in an Eulerian discretization, the material and the mesh are not connected and the mesh is fixed in space. The Figure 5.5 shows a visualization of the two mentioned phenomenons. ALE is a combination of both lagrangian and eulerian approaches. It takes some of the advantages from both methods. By using ALE, the mesh moves independently from the material, providing versatility in handling problems with large deformations or fluid-structure interactions. All these methods are within the field of FEA, and are teqniques for breaking the structure down into smaller, manageable elements.

(a) Lagrangian *(b) Eulerian*

Figure 5.5: Behaviour of mesh and material [1]

The above mentioned methods discretize the geometry by meshing the system or structure into smaller elements. There are also meshfree methods such as smoothed particle hydrodynamics (SPH) or discrete element method (DEM). The SPH approach is well-suited for problems involving fluid dynamics and large deformations and it could also be used for modeling granular materials. In this method, the material is represented as a continuum consisting of individual particles. A smooth interpolation is used to relate the distribution of stresses and strains between the particles.

In the discrete element method, each element is treated as a separate entity and the material is considered to be discontinuous. DEM is suitable for systems in which the interaction of the granular elements plays a significant role. In fig 5.6, a visualization of discrete elements is provided. In both the SPH and DEM approaches, the size distribution can be specified, which is favorable for soil modeling. In the same manner to FEA, DEM and SPH are numerical methods used for calculating the resulting forces and stresses from the particle interactions.

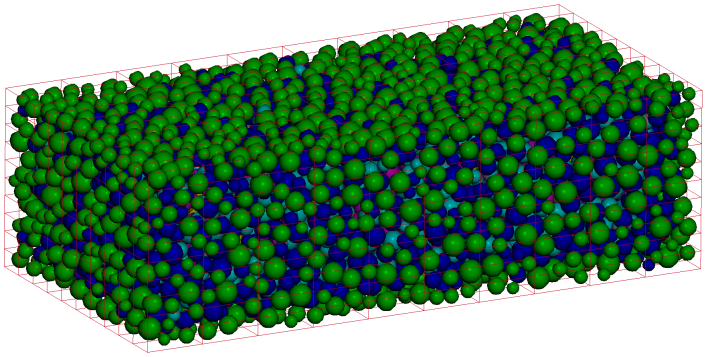

Figure 5.6: Discrete elements

When deciding which discretisation approach to use, there are as above mentioned several moments to take into consideration. By assuming that the contact area between the dropping object and the pipeline is much smaller than the contact area between the soil and pipe, it is reasonable to expect a large deformation in the pipe and the displacement of the soil is relatively small. Taking this expectation into account, a lagrange discretization of the soil will in many cases give adequate results.

6 Modelling and Numerical Simulation in LS-DYNA

The simulations and modeling are performed using the LS-DYNA software. LS-DYNA is a general purpose software for the simulation of impact, crash and other types of accidental events. It can be used in many different engineering fields, such as dropped objects, fire simulation, and vehicle collision simulations. It was originally developed by LSTC in the 1970s and the company was acquired by ANSYS in 2019. In this thesis, the software is used for non-linear simulation of the pipeline's structural response. In this context, it has a wide range of capabilities and both implicit and explicit solvers are available. In addition, advanced element formulations and material models can be employed. Throughout the modeling, a system of consistent units is used. In the software, there are no default units, but the user has to use the same units in all the processes, and the units used in this thesis are outlined in table 6.1.

Table 6.1: Units

Parameter	Mass	Length	Time	Force	Stress	Energy
Unit	kg	m	s	N	Pa	J

6.1 Mesh Sensitivity

During the literature review with this thesis, it has been decided to use other researchers work when choosing the mesh size for the different geometries modeled. Figure 6.1 shows the resulting dent depth for different mesh sizes, and the work is done in a paper by F. Jiang et al. [7]. The figure shows that the results start to converge for mesh sizes smaller than 0.05D, where D is the diameter of the pipeline. As the setup, with a pipeline, soil and dropping object was quite similar to the model developed in this thesis, the result of the mesh sensitivity study by was found sufficient to be used in this thesis. This resulted in a mesh size as shown in equation 6.1.

$$Mesh\,Size = 0.05 \cdot D = 25.4mm \tag{6.1}$$

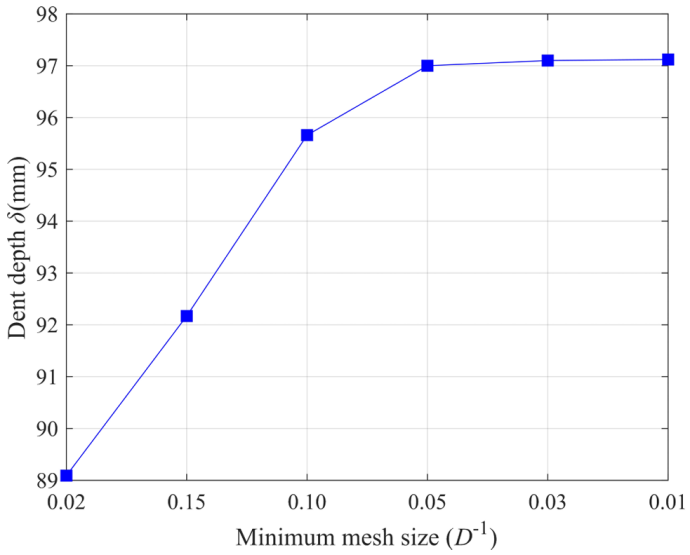

Figure 6.1: Mesh sensivity [7]

The stresses and strains are expected to be of larger magnitudes at the impacted area, and therefore the mesh is modeled with smaller elements in this region compared to the remaining area. In this case, the impact area is in the center of the pipeline. Additionally, the contact area between the pipeline bottom and the soil will also experience higher stresses and strains and is modeled with a smaller mesh size. In transition zones of different mesh sizes it is important to have a continuous mesh. This implies that each node must be connected to a node on the adjacent element. Neighboring elements then share common nodes, and this leads to more accurate results, as the transfer of stresses and strains is done at the nodes, and then there is compatibility between the elements. Figure 6.2 illustrates how the nodes are connected to each other in the transition between small and large mesh sizes.

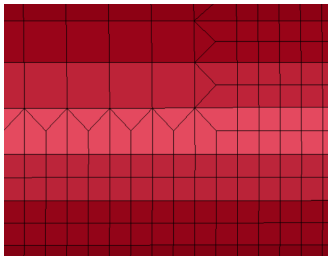

Figure 6.2: Mesh transition zone on pipeline

For modeling the pipeline non-contact areas, a mesh size of 50×50 mm was used. For the contact areas, a mesh size of 25×25 mm was used. For the tank with the handling frame, elements of 25×25 mm was used. For the soil, elements of 25×25×25 mm was used.

6.2 Geometry Modeling

6.2.1 Pipeline

The pipeline is modeled as a 20-inch circular pipe with a wall thickness of 50 mm. The dimensions were based on commonly used values for subsea pipelines. However, it is notable that there is a wide range in the dimensions used in the industry, and this is only one of many possible combinations of wall thickness and diameter that could be analyzed. An overview of the dimensions of the three different pipelines considered is given in table 6.2. The nominal diameter is the same in all cases, but the varying wall thickness results in different inner and outer diameter for the studied pipelines. In all the cases, the pipeline length was set to 7 meters with the intention of covering the full length of the tank during the impact.

Table 6.2: Pipeline dimensions

Dimension	**Pipe 1 [mm]**	**Pipe 2 [mm]**	**Pipe 3 [mm]**
Nominal diameter	508	508	508
Inner diameter	458	482.6	495.3
Outer diameter	558	533.4	520.7
Wall thickness	50.0	25.4	12.7
Length	7000	7000	7000

Figure 6.3 shows one of the pipelines in full length. In the figure, the thickness of the pipeline

wall is visible. As mentioned before, the pipeline is created by shell elements, and it is the thickness of the shell elements that create the visible wall thickness. Further details of the pipelines can be found in Appendix A with cross sectional drawings in addition to side view drawings.

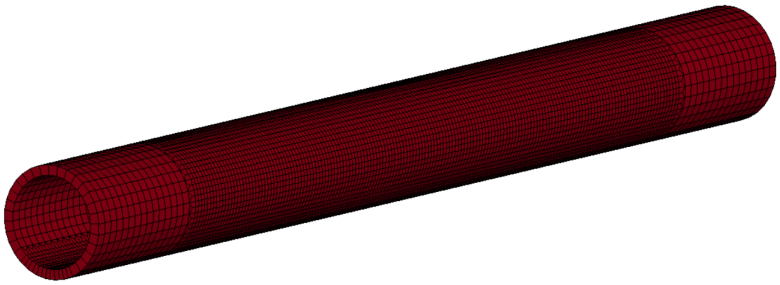

Figure 6.3: Pipeline

6.2.2 Tank and Handling Frame

The tank with the frame was modeled with outer dimensions of 2.95×1.85×2.3 meters. The wall thickness of the tank itself is 4 mm. It should be noted that the work to create the geometry of the tank model was not done in this thesis and the model was provided by the supervisor of the thesis. In Figure 6.4, two drawings with unmeshed and meshed geometry are provided.

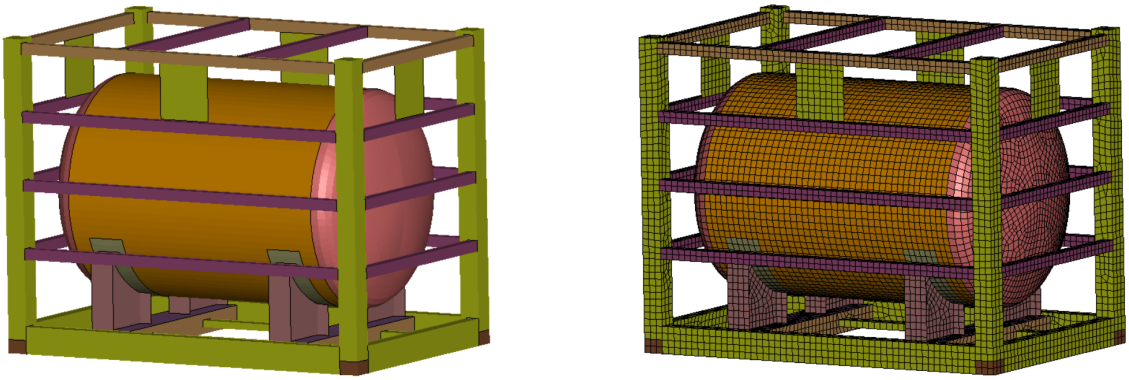

(a) Unmeshed *(b) Meshed*

Figure 6.4: Tank and frame model

A more detailed and comprehensive overview of the dimensions and thicknesses are provided in Table 6.3. The main frame, which is modeled with a green color in the figure, has a thickness of 6 mm. In comparison, the bracings inside the frame have a thickness of 5 mm, meaning that the bracings are considered to be the weakest parts of the frame. Detailed drawings can be found in appendix B.

Table 6.3: Tank with frame dimensions

Dimension	Tank with frame [mm]
Length	2 950
Width	1 850
Height	2 300
Frame section	150 x 150
Frame thickness	6
Bracing section	80 x 80
Bracing thickness	5
Tank thickness	4

6.3 Material Modeling

During the work of this thesis, there have been used different materials. Steel of grade S355 was utilized for the pipeline, while steel of grade S275 was employed for the tank. For the soil, two different types have been used and several soil material models have been studied to find the most suitable for the simulation.

6.3.1 Structural Steel

The steel used in the thesis is modeled using a custom-made stress strain curve based on the proposed stress values and the corresponding strain values in DNV-RP-C208. The material model for the steel was *Linear Piecewise Plasticity* and this is one of the most commonly and primarily used material models in LS-DYNA for modeling steel and similar materials. It is relatively basic in terms of useability and it is applicable for many engineering purposes. It is also possible to easily create custom-made stress and strain points on the material's stress-strain curve. By using this technique of defining individual points, the software will then evaluate the stress-strain curve as linear segments.

In the simulations, it is expected that large deformations will occur and this expectation is of interest when it comes to choosing the values of the load-displacement curve. The large deformation will induce changes in the cross-sectional area, meaning that true stress-strain values are more appropriate than engineering stress-strain values. The equations for calculating true stress and true strain values are given in equation 6.2 and 6.3 respectively.

$$\sigma_t = \sigma_e \left(\varepsilon_e + 1\right) \tag{6.2}$$

$$\varepsilon_t = ln\left(1 + \varepsilon_e\right) \tag{6.3}$$

The recommended method in DNV-RP-C208 for modeling stress-strain values in non-linear analysis is to use a combination of two linear segments, as shown in Figure 6.6, and a curve specified by equation 6.4. For strain values larger than $\varepsilon_{p,y2}$, the stress values are calculated with the expression given in equation 6.4.

$$\sigma = K\left(\varepsilon_p + \left(\frac{\sigma_{yield,2}}{K}\right)^{1/n} - \varepsilon_{p,y2}\right)^n \; for\, \varepsilon_p > \varepsilon_{p,y2} \tag{6.4}$$

The code also proposes to use true stress and true strain values, as there might be large deformations resulting in changing cross-sectional areas. Table 6.4 provides the necessary values for creating the stress-strain curves for modeling S355 Structural Steel. The table is created based on the values in table 4-4 in DNV-RP-C208 which offers true stress and true strain values. The tank was modeled with thicknesses below 16 mm and the pipeline is modeled with thicknesses of 12.7 mm, 25.4 mm and 50.0mm which based on the table required different stress-strain curves.

Table 6.4: Stress-strain curve parameters for S355

Parameter	**Thickness (mm)**		
	t≤16	$16 < t \leq 40$	$40 < t \leq 63$
E [MPa]	210000	210000	210000
σ_{prop} [MPa]	320.0	311.0	301.9
σ_{yield} [MPa]	357.0	346.9	336.9
$\sigma_{yield,2}$ [MPa]	363.3	353.1	342.9
$\varepsilon_{p,y1}$	0.004	0.004	0.004
$\varepsilon_{p,y2}$	0.015	0.015	0.015
K	740	740	725
n	0.166	0.166	0.166

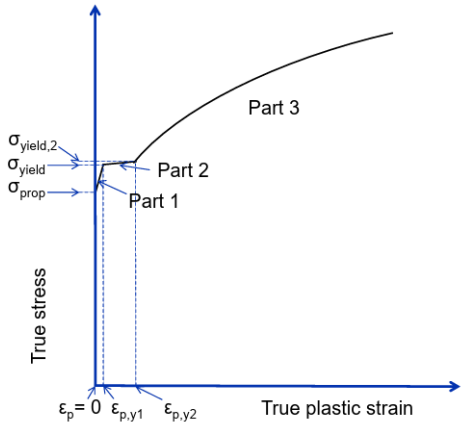

Figure 6.5: Recommended stress-strain curve [15]

The stress-strain curve for steel of grade S355 is given in Figure 6.6 and the stress-strain curve for steel of grade S275 is given in Figure 6.7. For the tank all the wall thicknesses of the sections were within the same thickness limitations. In addition to the stress-strain curve the material model used requires material properties such as density and poisons ratio. Density of the steel was set to 7850 kg/m^3 and the poisson's ratio was set to 0.3.

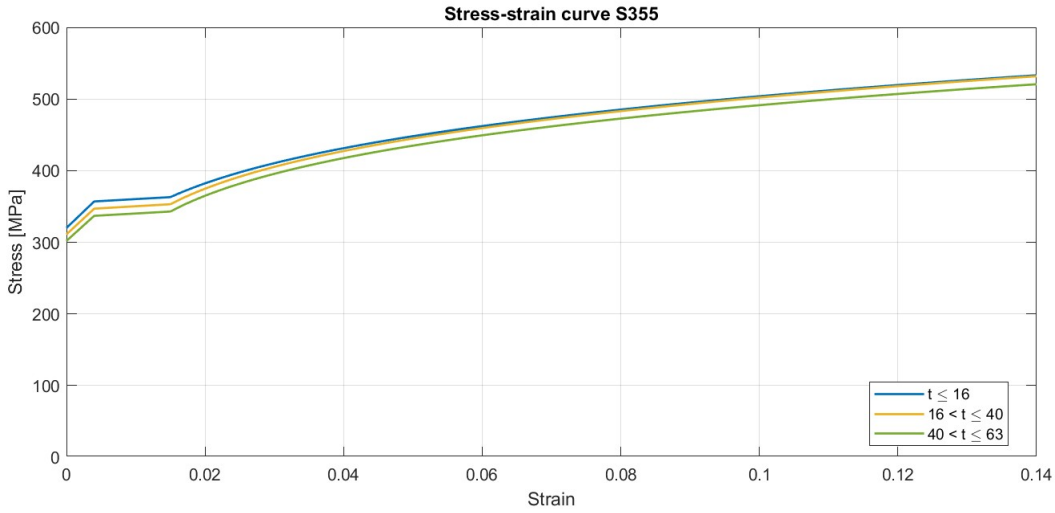

Figure 6.6: Stress strain curves for S355

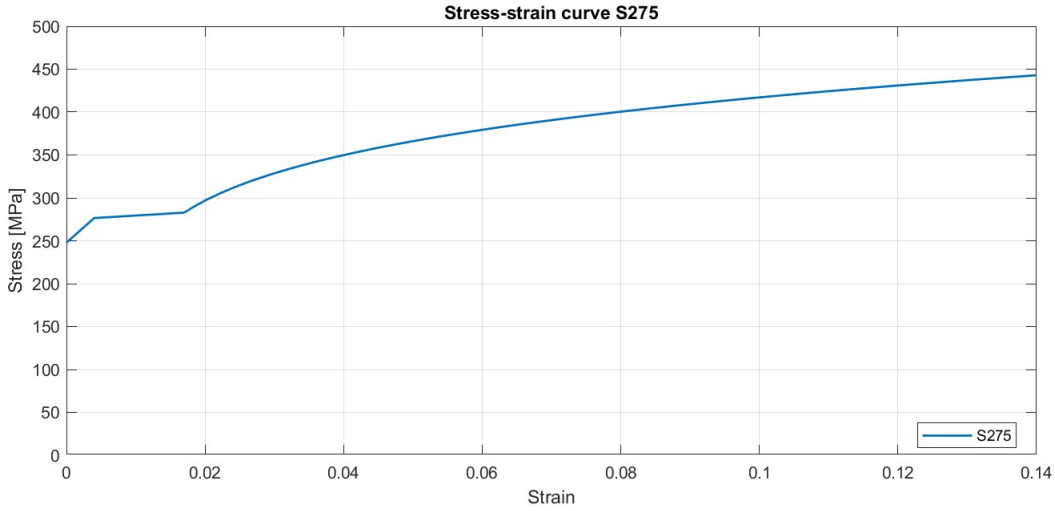

Figure 6.7: Stress strain curves for S275

6.3.2 Soil

Two distinct soil models, clay and natural sand, were employed for soil modeling. The two soil models were obtained from research papers in which the LS-DYNA software was used. In addition to the soil models used, an attempt to create a soil model for marine soils was carried out. The model was based upon data obtained from research papers. The work resulted in very large and unnatural displacement values. It was therefore decided that the marine clay model was not appropiate to use in the thesis and only the already established material clay and natural sand were used. The inputs required for the material model is given in Table 6.5. In the software library, the material model used is identified as *Mat Soil And Foam*.

Table 6.5: Required input parameters

Input	Description
RO	Density
G	Shear Modulus
BULK	Bulk Modulus
A0, A1, A2	Yield function constants
PC	Pressure cutoff for tensile fracture
EPS1,..	Volumetric strain values
P1,..	Pressures

Table 6.5 shows the required input parameters for the material model used. In addition to common material properties such as shear modulus and bulk modulus, the coefficients from the yield function are also required. The parameters EPS1,.. and P1,.. are pairs of stress and corresponding volumetric strain values. In accordance with the material manual, the natural logarithm of the volumetric strain values should be used. The specific values for different soil materials is given in Table 6.6. Dry sand and dry clay are found not to be appropriate for simulating seabed soils, as seabed soils are water-saturated. However, the values are included in the table for comparison. The data for the Clay and Natural Sand were obtained through the references [3] and [18] respectively.

Table 6.6: Soil material inputs

Soil type	Density	Shear Modulus	Bulk Modulus	$\mathbf{a_0}$[$\mathbf{Pa^2}$]	$\mathbf{a_1}$[Pa]	$\mathbf{a_2}$[−]
Clay	1700 kg/m^3	2.524 MPa	4.673 MPa	1.0e9	4900	0.0079
Natural sand	1710 kg/m^3	1.6 GPa	2.5 GPa	3.3e14	0	0
Dry sand	1390 kg/m^3	2.620 MPa	9.463 MPa	3.0e8	2.53e4	0.535
Sandy loam	1470 kg/m^3	1.12 MPa	4.44 MPa	2.37e6	830	0.0726
Dry clay	1980 kg/m^3	5.2 GPa	11.38 GPa	7.5e13	8.26e6	0.227

According to a Ph.D. thesis by A. Wright [20], the input parameters a_0, a_1 and a_2 can be determined by using the relations given in equation 6.5 - 6.6. In the equations, c corresponds to the cohesion of the soil and ϕ corresponds to the internal friction.

$$a_0 = \frac{4c^2}{3} \tag{6.5}$$

$$a_1 = \frac{8c \cdot \tan\phi}{3} \tag{6.6}$$

$$a_2 = \frac{4 \cdot \tan^2\phi}{3} \tag{6.7}$$

From the LS-DYNA material manual [2] the yield stress of the material model can be obtained through the expression given in equation 6.8.

$$\sigma_y = [3(a_0 + a_1 p + a_2 p^2)]^{\frac{1}{2}} \tag{6.8}$$

In addition to the parameters described in table 6.6, the stress and corresponding strain values are required to fully describe the soil material models.

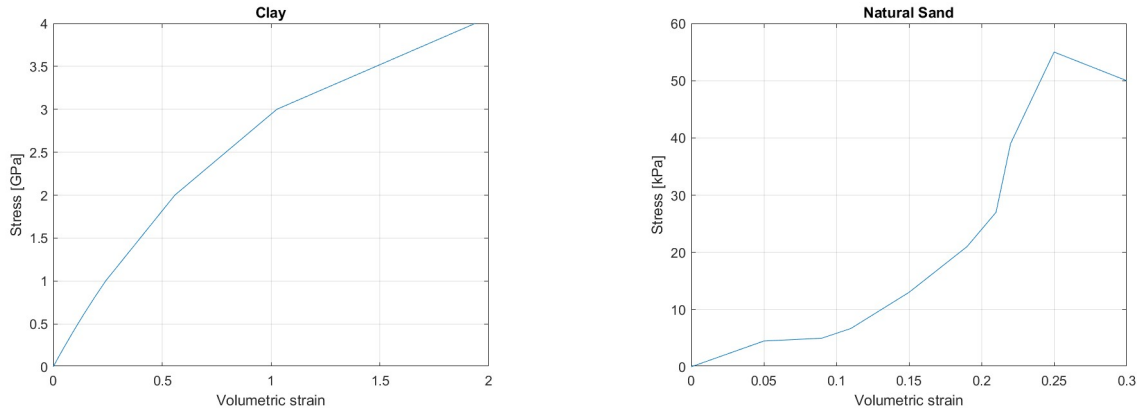

(a) Clay *(b) Natural sand*

Figure 6.8: Stress - volumetric strain values

In the software, the stress and volumetric strain data have to be given as individual points and in Table 6.7 and 6.8 the actual stress and volumetric strain values used are provided.

Table 6.7: Stress and strain values for clay (Stress units: Pa)

EPS1	**EPS2**	**EPS3**	**EPS4**	**EPS5**	**EPS6**	**EPS7**	**EPS8**	**EPS9**	**EPS10**
0.0	0.0216	0.0437	0.0895	0.1374	0.1878	0.2408	0.5586	1.0272	1.9380
P1	**P2**	**P3**	**P4**	**P5**	**P6**	**P7**	**P8**	**P9**	**P10**
0.0	1e8	2e8	4e8	6e8	8e8	1e9	2e9	3e9	4e9

Table 6.8: Stress and strain values for natural sand (Stress units: Pa)

EPS1	**EPS2**	**EPS3**	**EPS4**	**EPS5**	**EPS6**	**EPS7**	**EPS8**	**EPS9**	**EPS10**
0.0	0.05	0.09	0.11	0.15	0.19	0.21	0.22	0.25	0.30
P1	**P2**	**P3**	**P4**	**P5**	**P6**	**P7**	**P8**	**P9**	**P10**
0.0	4500	5000	6700	1.3e4	2.1e4	2.7e4	3.9e4	5.5e9	5.0e9

6.4 Position Arrangements

In addition to the geometry and properties of the material previously discussed, information about the impact position and analysis setup is required to fully describe the simulations. The two most critical positions of the tank and the pipeline are identified as flat impact and edge impact according to the two subplots in Figure 6.9. This evaluation is done based on the geometry of the tank and the pipeline, where the contact area and the thickness of the frame are taken into account.

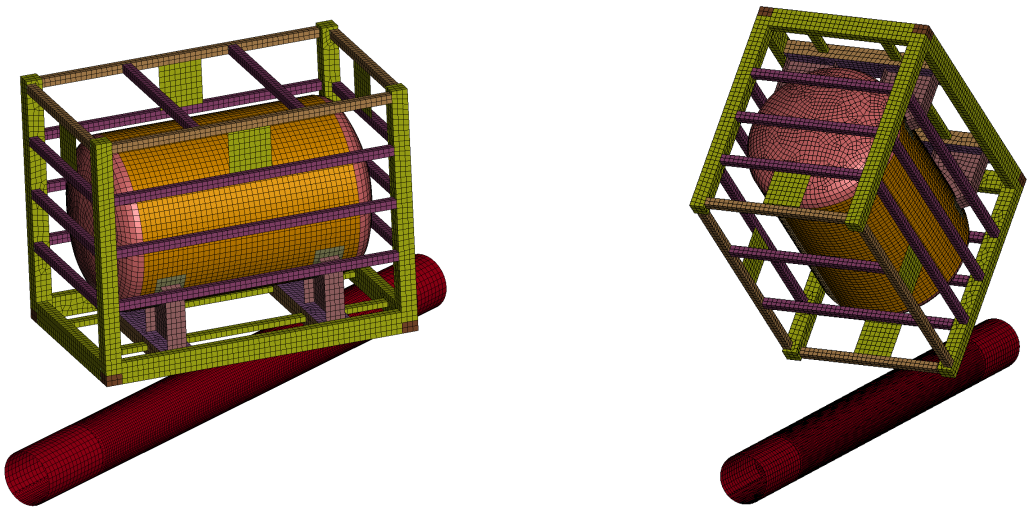

(a) Flat impact *(b) Edge impact*

Figure 6.9: Impact arrangements

The notation "flat impact" and "edge impact" will be used throughout the thesis to differentiate between the impact scenarios. In terms of the structural integrity of the tank, the edge impact is expected to cause the most permanent deformation due to a small contact area. Similarly for the pipeline, the small contact area that follows this arrangement is expected to cause the most structural damage to the pipeline.

6.5 Boundary Conditions

For the simulations with soil, boundary conditions have been applied to the soil according to what is shown in Figure 6.10. The blue area indicates the nodes to which the boundary conditions have been applied. The nodes were fully restrained, meaning that any translational or rotational motion was restricted.

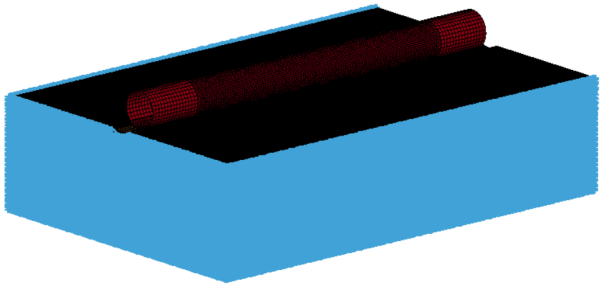

Figure 6.10: Boundary conditions of the soil

In addition to the fixed nodes at the soil, a non-reflecting boundary condition has also been employed. The non-reflecting boundary condition prevents the stress waves to be reflected when it reaches the boundaries. This implies that when the stress waves hit the nodes to which this condition is assigned, the waves leave the simulation without bouncing back. In the simulations, non-reflecting boundary conditions have been assigned to the same nodes as the fixed nodes marked with blue in Figure 6.10.

For the rigid simulations, boundary conditions have been applied to the bottom of the pipeline. The nodes which were expected to be in contact with the seabed have been fixed in both

translational and rotational degrees of freedom. A figure of the cross-section of the pipeline with the fixed nodes is shown in Figure 6.11. The fixed nodes are marked with green dots.

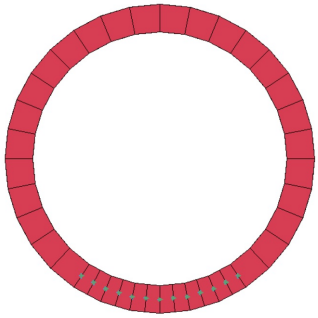

Figure 6.11: Rigid seabed boundary conditions

6.6 Other Simulation Details and Keyword Overview

Other analysis information that has not been covered so far includes gravity, simulation time, and frictional coefficients. The simulation time was set to 0.7 seconds and the motion of the tank started at 0.2 seconds. During the simulation time of 0.7 seconds, the impact occurs, and the tank starts to rebound. Gravity is initialized and applied to both the pipeline and the soil, and no gravity is added to the tank. The movement of the tank is only governed by the initial velocity of 6.3 m/s which was calculated in section 3.1.

Additionally, friction coefficients for the contact between the intersecting bodies is specified and the value used was 0.3. Lastly, a summary of the keywords used is provided in Table 6.9. The table does not show keywords related to topics discussed previously in the thesis, such as material properties and element formulations.

Table 6.9: Keyword overview

Keyword	**Description**
*CONTROL_ENERGY	Specifies which energy should be included
*CONTROL_TERMINATION	Specifies the simulation time
*CONTROL_TIMESTEP	Set timestep and safety factor
*DATABASE_ASCII_OPTION	Used for write the time history data
*DATABASE_BINARY_D3PLOT	Define time interval between output
*DATABASE_HISTORY_NODE_SET	Track the positions of nodes
*BONDARY_SPC_SET	Boundary conditions and constraints
*SURFACE_TO_SURFACE	Contact between pipe-soil and pipe-object
*SINGLE_SURFACE	Self-contact within the frame
*INITIAL_VELOCITY_GENERATION	Applying the terminal velocity to the tank

7 Simulation Results

In this chapter, the results of the simulations will be presented. In the context of impact analysis, plots of internal energy and contact force are essential to understand the structural response. Additionally, contour plots of stress and strain will be given, as well as displacement and deformation plots. The plots focus on the structural behavior of the pipe for different types of soil and also on how the different wall thicknesses affected the results.

Table 7.1 provides an overview of the different simulations performed in this thesis. The simulations are divided into different series, where each has a specific characteristic. All simulations in series 1 have a pipe wall thickness of 50mm. Similarly, series 2 shares the common value of pipe wall thickness of 25.4 mm. For the series 3, all simulations have a rigid seabed. Diagrams showing the most important findings are provided in the coming subsections to summarize the results of the mentioned simulations.

Table 7.1: Simulation overview

Serie	Simulation	Soil Type	Tank Impact	Thickness Pipe [mm]
Serie 1	1	Clay	Edge	50.0
	2	Clay	Flat	50.0
	3	Natural sand	Edge	50.0
	4	Natural sand	Flat	50.0
Serie 2	5	Clay	Edge	25.4
	6	Clay	Flat	25.4
	7	Natural sand	Edge	25.4
	8	Natural sand	Flat	25.4
Serie 3	9	Rigid	Edge	50.0
	10	Rigid	Edge	25.4
	11	Rigid	Edge	12.7

7.1 Stress Contour Plots

7.1.1 Tank

Figure 7.1 shows the resulting von Mises stress distribution of the tank. As seen in the figure, the frame is experiencing high deformation, and also the tank itself is deforming. The picture is obtained from Simulation 3, which was the simulation with the highest internal tank energy, and hence the simulation with the most deformation. The progression of damage can be seen as three different time points are presented. The stress value ranges provided to the right of the three figures are the same for all three simulations to improve the comparability of the figures.

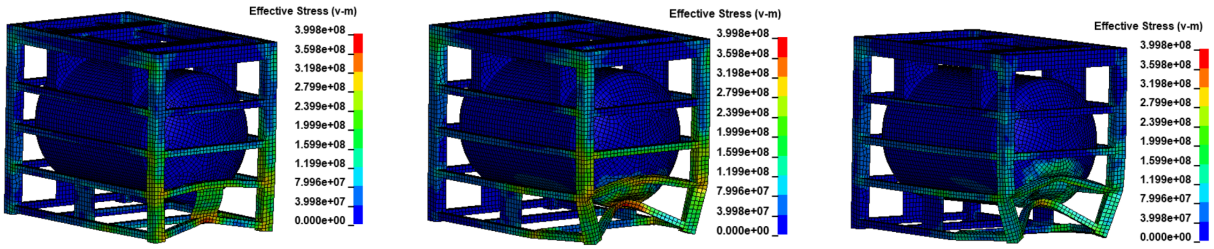

(a) t = 0.26s *(b) t = 0.32s* *(c) t = 0.7s*

Figure 7.1: Damage propagation of the tank

7.1.2 Pipeline

In Figure 7.2, stress contour plots of the pipe in Simulation 1, 6 and 7 is provided. Simulation 1 and 7 were both edge impacts and the resulting Von Mises stress plots are similar to each other with respect to the location of stresses, but in terms of stress magnitude, the values have some deviations. For the Simulation 1 the maximum stress was 28,6 MPa and for the Simulation 7 the maximum stress was 147,6 MPa. The Simulation 6 is according to table 7.1 a flat impact, and compared to the Simulation 1 and 7, the stress distribution has changed and is distributed throughout the whole pipe and with the maximum stress occurring at the ends where the main frame of the tank hit the pipe. In the Simulation 6 the maximum Von Mises equivalent stress was 207,6 MPa. In all cases in series 1 and 2, no visible local damage occurred, and therefore the three provided stress distributions do not show any deformation.

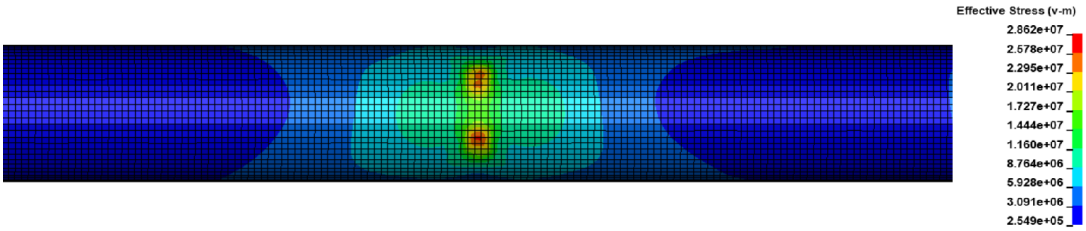

(a) Simulation 1

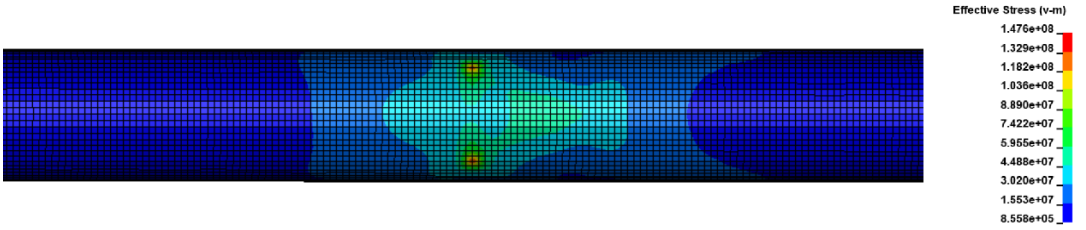

(b) Simulation 7

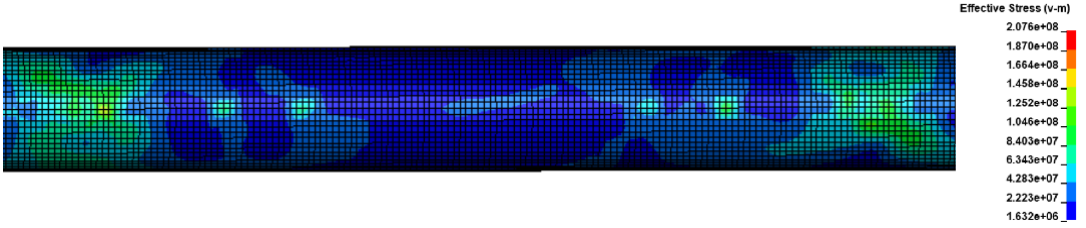

(c) Simulation 6

Figure 7.2: Von Mises Stress for 3 different simulations

Even none of the pipes in the above figure resulted in high stress concentrations for local damage to occur, the simulations in series 3 did. The stress contour plots from these simulations are available in section 7.9, together with the other results of the special rigid seabed simulations.

7.2 Energy Distribution

Figure 7.3 (a) shows how the different energy varies with time. The left subplot have line graphs to show individual energies, making it easier to observe the specific changes in each type. The lines represent the energy of the system, and not only for individual parts. As it is a closed system, no energy will disappear or be generated, except for the added kinetic dropping object energy. The right subplot filled areas indicate that while the distribution of energy types changes, the total energy is conserved over time, as shown by the constant total energy level.

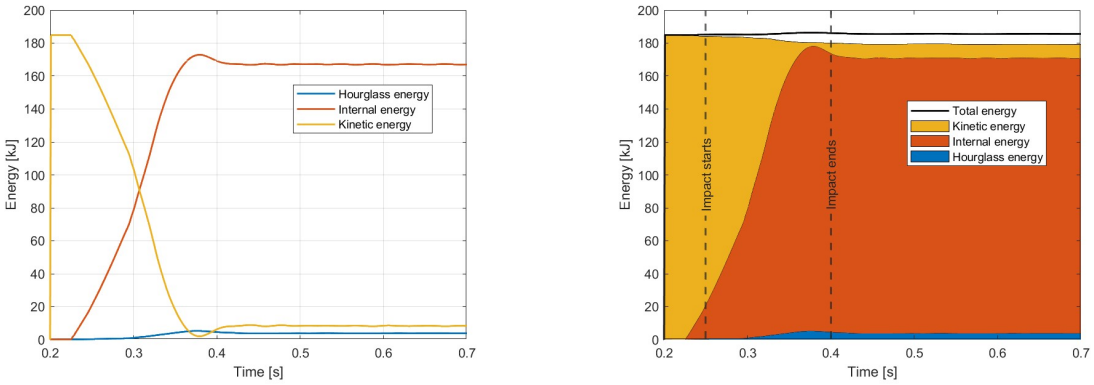

(a) Individually *(b) Summation*

Figure 7.3: Energy distribution

According to the LS-DYNA manual, the total energy is composed by internal energy, kinetic energy, contact energy, hourglass energy, system damping energy and rigidwall energy. In Figure 7.3 (b), the gap between the colored area and the total energy is then the sum of the contact energy, system damping energy, and the rigidwall energy. The two vertical dotted lines represent the time at when the impact between the two objects starts and ends. During the impact, it can be seen that the kinetic energy decreases significantly and simultanously, the internal energy increases. It can also be seen that within this timeframe, the minimum kinetic energy occurs, which corresponds to the moment when the tank starts to rebound. Additionally, it can be observed that the hourglass energy is at its maximum during the contact phase.

7.3 Hourglass Energy

To have sufficient small hourglass energy relatively to the internal energy is important to have reliable and trustable results. If this is not the case, there might be a possibility that the deformation is not accounted for when calculating the stress and strain, as described in Section 5.6. For visualization a plot showing global internal energy and global hourglass energy for one random simulation is provided in Figure 7.4. From the figure, it can be seen that the maximum hourglass energy is approximately 10 % of the internal energy. The other simulations also exhibit equivalent and similar shapes in the hourglass and internal energy diagrams, therefore, they are not included in the thesis.

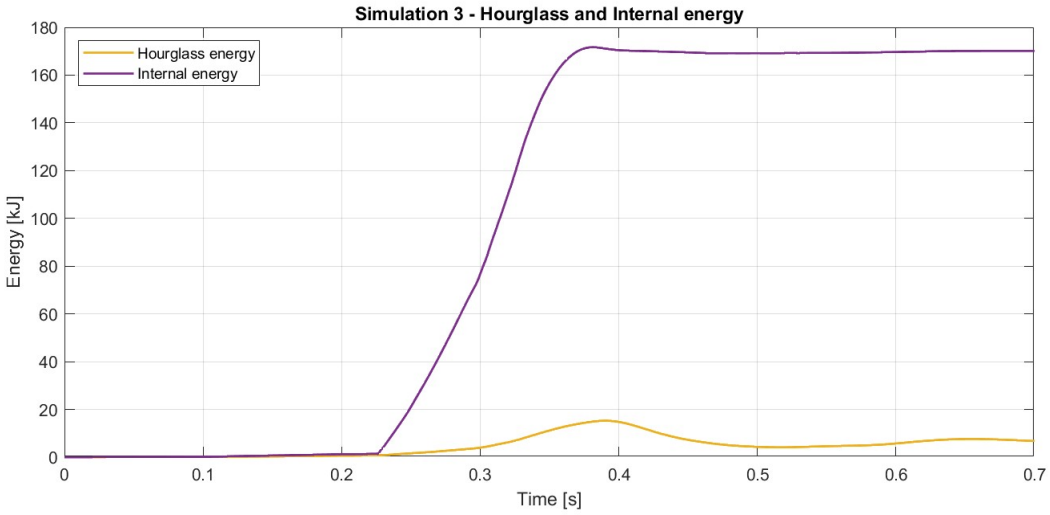

Figure 7.4: Hourglass and internal energy - global

As an alternative, a bar chart showing the ratios of the maximum hourglass energy to the maximum internal energy is provided in Figure 7.5. This diagram reveals that all the simulations have ratios of hourglass to total energy of less than 15 %. Simulations 1 and 5 have ratios below 5 %, which is found to be sufficient to have reliable results, although smaller ratios would have resulted in even more precise results. In the other cases, the ratios are somewhat more than what is preferable. It should be noted that without the addition of the hourglass control to the soil elements, described in Section 5.6, the hourglass to total energy values would have been significantly larger.

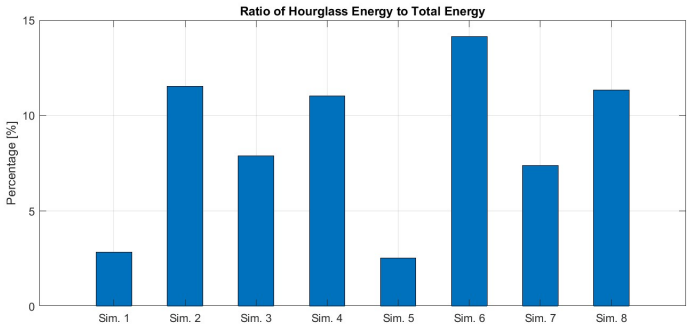

Figure 7.5: Hourglass energy as percentage of total energy

7.4 Kinetic Energy

The kinetic energy in Figure 7.6 represents the total motion of all parts in the simulations. The figure reveals information about the energy and velocity of the rebound of the tank. As the figure shows, the kinetic energy at the end of the simulation is almost the same. This implies that the velocity of the tank in the rebound is the same in all the simulations.

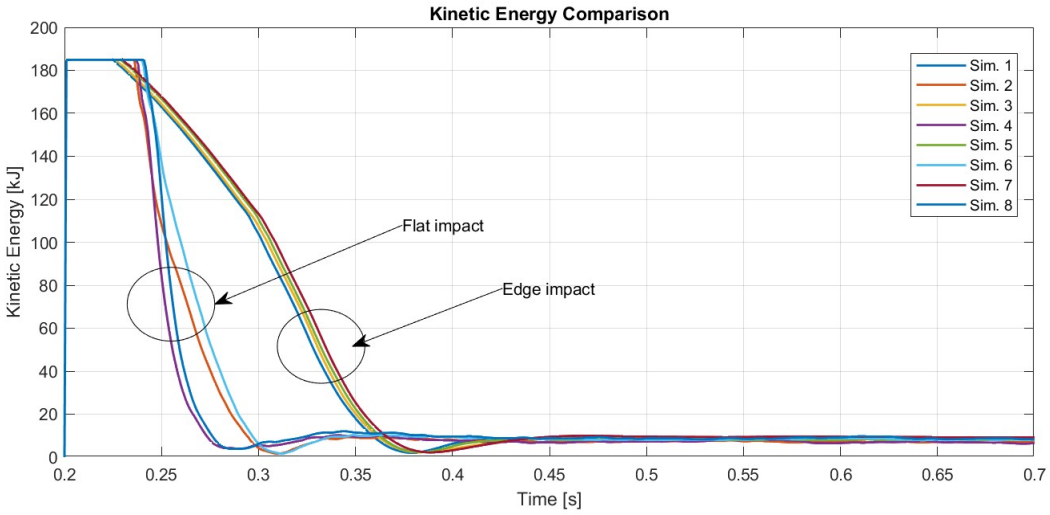

Figure 7.6: Comparison of kinetic energy

From the figure it can be observed that there is a clear distinction in the kinetic energy curves for the flat and edge impacts. The flat impact's kinetic energy is more rapidly decreasing and varies more than the edge impacts. This can be explained by the fact that the edge impacts are dampened over a longer period of time due to the lower strength of the tank compared to a flat impact.

7.5 Imapct Force

As the soil under the pipeline is essential for the pipeline structural response, a diagram showing the time development of the force between the dropping object and the pipeline is given in Figure 7.7. There are only forces present when the two bodies are in contact, and for this reason the time-axis is shortened and the whole simulation time is not visible. With respect to the structural integrity of the tank, there are two different tank positions of interest, one being the most critical one and as mentioned before this is the edge impact and the other scenario is flat impact.

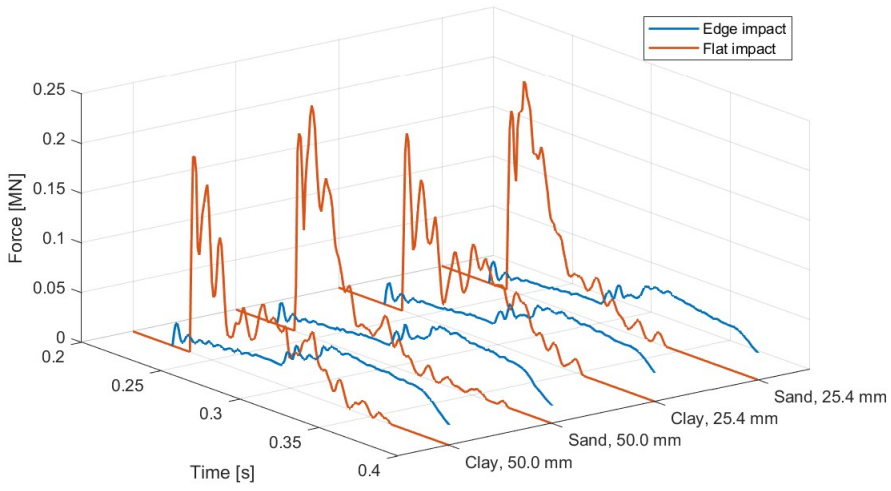

Figure 7.7: Impact force

The diagram shows that for both soil types, there is an considerable difference in the maximum force between edge and flat impact. This is as expected as the area of contact is smaller for the edge impact, which should result in a larger force magnitude when the impact energy is the same. In order to better visualize the differences between the lines in Figure 7.7, a 2-dimensional plot of the same lines is provided in Figure 7.8.

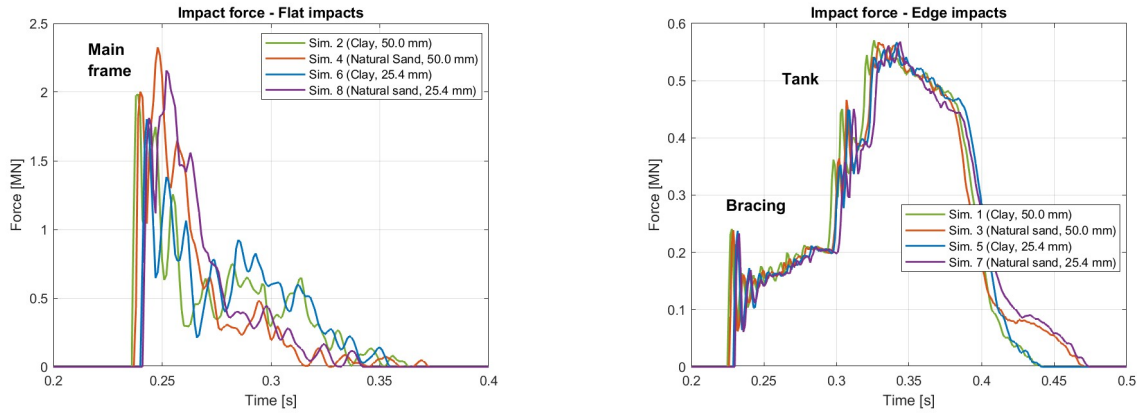

(a) Flat impacts *(b) Edge impacts*

Figure 7.8: Impact force

In Figure 7.8 (a) the contact force in the flat impact simulations are provided. According to the position arrangements, the flat impacts hit the pipeline with the main frame. This resulted in one characteristic peak in the impact force diagram and is in the figure marked by "Main frame". The reason of only one significant peak occurring is that the main frame and the pipeline have high strengths, and as a consequence no large localized deformation occured. This implies that the energy associated with the impact is dissipated in a short period of time and a large force magnitude occurs. In all four cases, the maximum contact force varies around 2.0 MN.

Figure 7.8 (b) shows a comparison of the edge impacts. The characteristics of the peaks in the plot can be described by the geometry of the tank. The first peak occurring at 0.23 seconds and marked as "Bracing" in the figure corresponds to the interaction between the bracing and the pipeline. Moving foreward, the force reduces slightly as the capacity of the brace is overcome before the impact force again begins to increase. In this region and which is marked as "Tank" in the figure, the pipeline interacts with the tank itself and the contact force increases to a value of 0.55 MN. The tank then starts to rebound and as a consequence the contact force start to gradually reduce until there is no contact between the two objects.

7.6 Internal Energy of the Pipeline

Figure 7.9 shows how the internal energy of the pipeline varies with the simulations. Most of the internal energy is not accumulated throughout the simulation, and there is, therefore, a small amount of plastic deformation in the pipelines. Figure 7.9 also shows that the most influencing parameter on the peak internal energy is the orientation of the dropping object. Similar to the force in Figure 7.8, the maximum values for internal energy are obtained for impacts where the tank his with a flat impact.

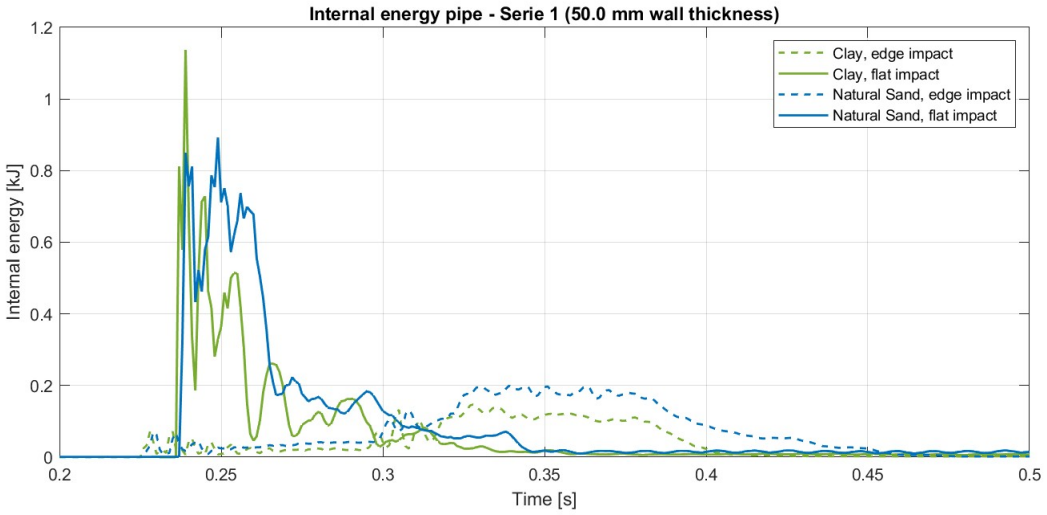

Figure 7.9: Internal energy of the pipeline (series 1)

When the wall thickness of the pipeline is reduced from 50.0 mm to 25.4 mm, the internal energy of the pipeline increases. This is shown in Figure 7.10 where the internal energy for the simulations from series 2 is plotted. Compared to the Figure 7.9, the values are increasing for both the two flat impact cases. Although there is an increase, it is still small compared to the impact energy, meaning that the internal energy dissipated in the pipeline is small compared to the systems total energy.

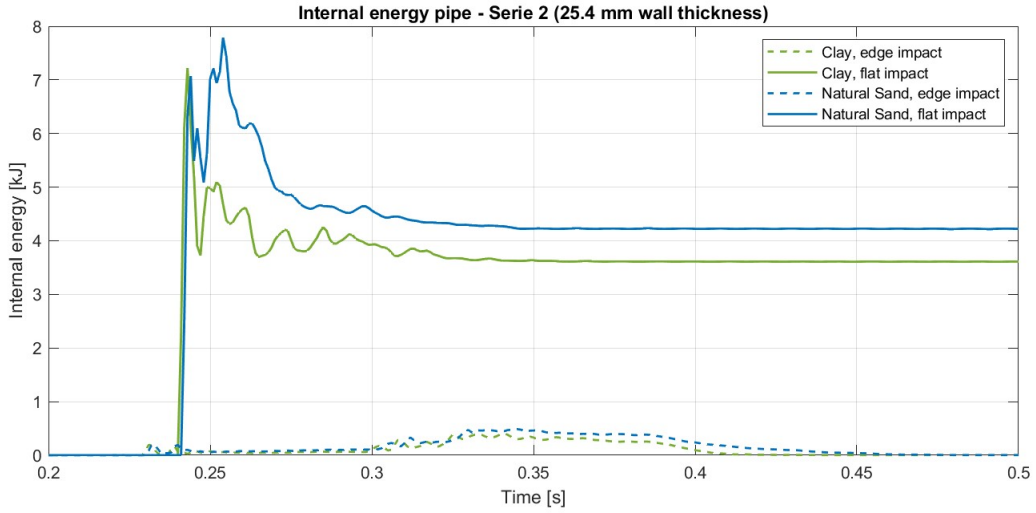

Figure 7.10: Internal energy of the pipeline (series 2)

7.7 Internal Energy of the Tank

In the Section 7.5, the internal energy of the tank and the impact force were presented. The force acting on the tank is the same as the force acting on the pipeline but in opposite directions, meaning that Figures 7.7 to 7.8 are applicable also for the tank.

The internal energy of the tank for the different scenarios is given in Figure 7.11. The figure shows that the maximum internal energy in the tank is obtained by Simulation 3, which was the simulation with natural sand and edge impact. However, the difference to the Simulation 1

(clay and edge impact) is very small. For the two simulations with flat impact, the difference is slightly more. Based on these observations, it can be seen that the most critical cases in terms of strain energy in the tank is the simulations with edge impacts. The reason of this can be explained by the difference in the geometry stiffness for the edge and flat impact.

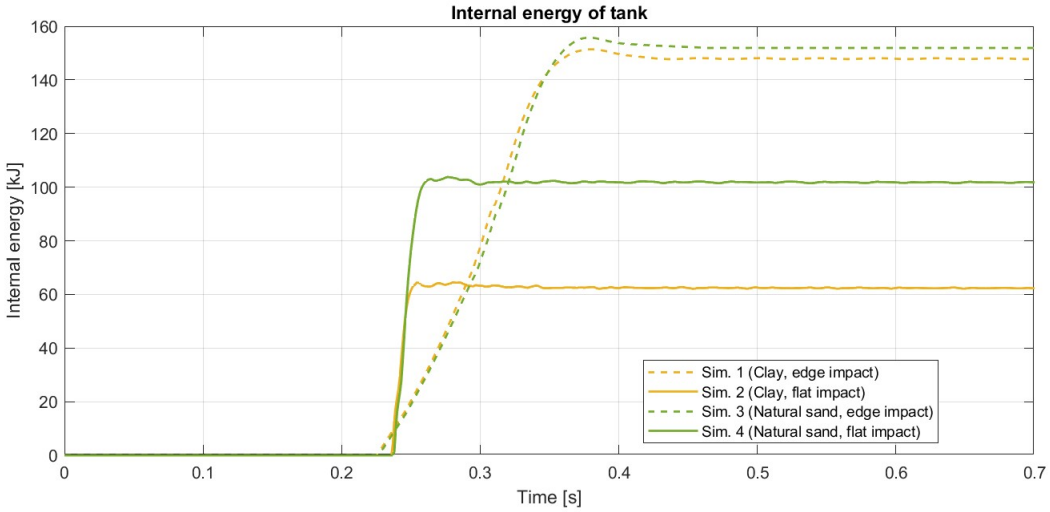

Figure 7.11: Internal energy of tank

The results of the internal energy of the tank from series 2, which was the simulations with wall thicknesses of 25.4 mm, are shown in Figure 7.12. The simulations with an edge impact, represented by dotted lines, are nearly identical to the edge impacts from series 1. The difference becomes visible for the flat impacts, where the smaller wall thickness results in less energy dissipation in the tank. This can be explained by more energy being dissipated in the pipeline as the diameter and structural capacity are reduced.

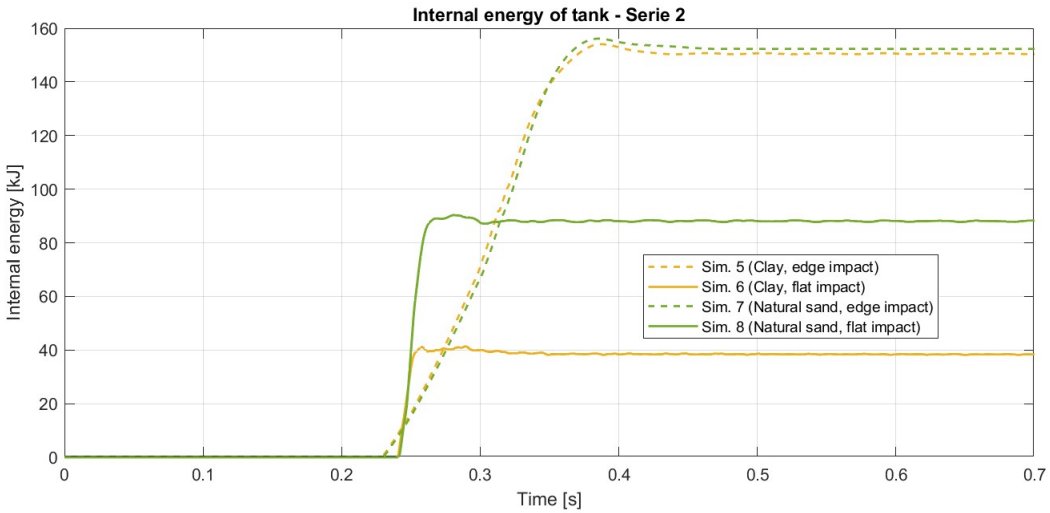

Figure 7.12: Internal energy of tank

7.8 Soil Displacement

To compare how the different scenarios affect the displacement of the soil, a diagram showing the vertical displacement of one of the soil elements is provided in Figure 7.13. Lines with the

same color correspond to the same soil properties and and dotted lines correspond to flat impact scenario and the solid lines correspond to edge impacts.

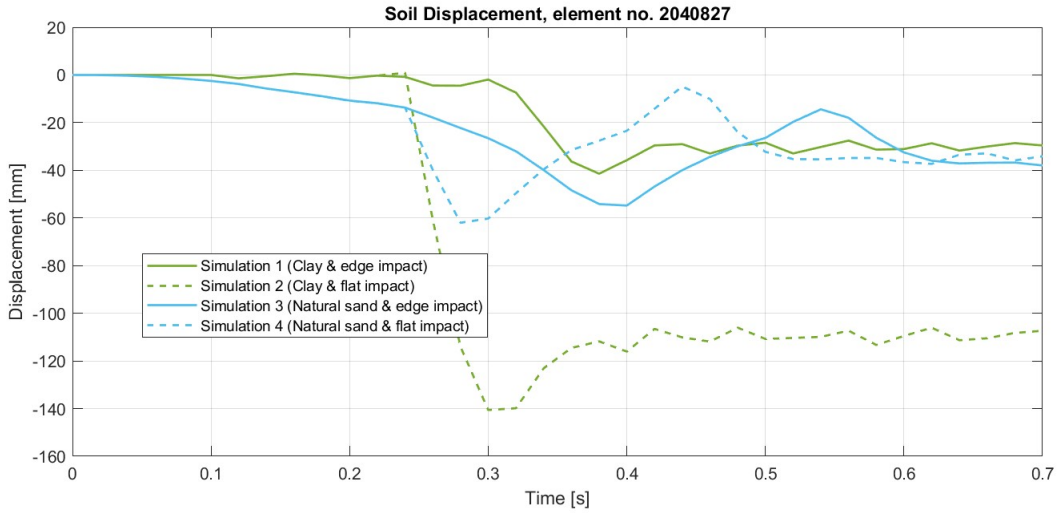

Figure 7.13: Soil displacement

To see the effect of a reduced wall thickness to the soil deformation, a plot with the differences in soil displacement between the series 1 and series 2 is provided in Figure 7.14. As seen from the figure, the differences is mostly below 5 mm, but the difference between Simulation 2 and 6 is somewhat more. This in itself indicates a slight dependence of wall thickness to the soil displacement. Because there is only one observation arguing in this direction, it is difficult to conclude about this dependency.

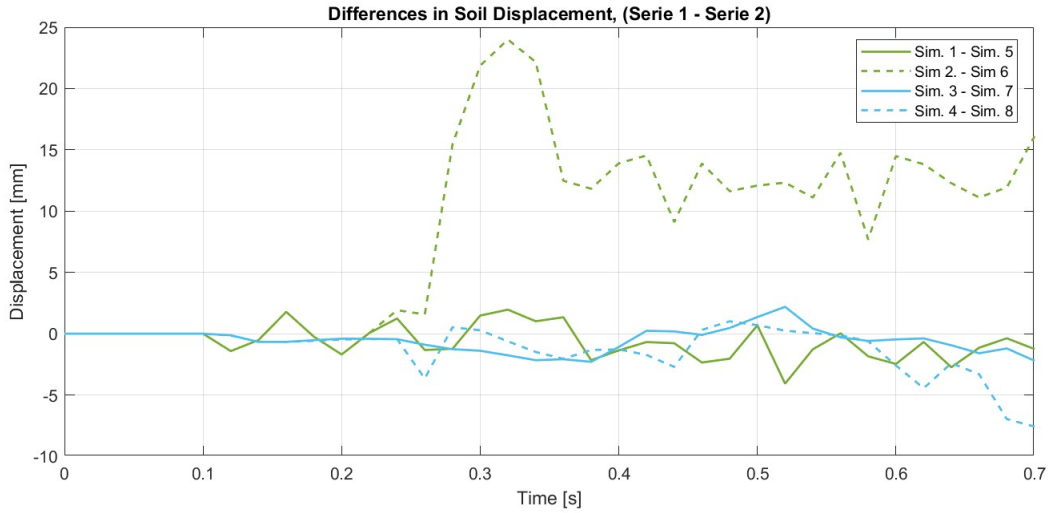

Figure 7.14: Soil displacement difference

The above Figures 7.13 and 7.14 represents only the element with the most displacement. To better visualize the displacement of the whole soil, Figure 7.15 provides a contour plot showing the resultant displacement. The units of the displacement are meters. As expected, the soil displacement is largest right below the pipeline. The figure does not represent the total simulation time, but is taken for two different time points. It should also be noted that the figure

represents Simulation 2, which resulted in the largest soil displacement according to Figure 7.13.

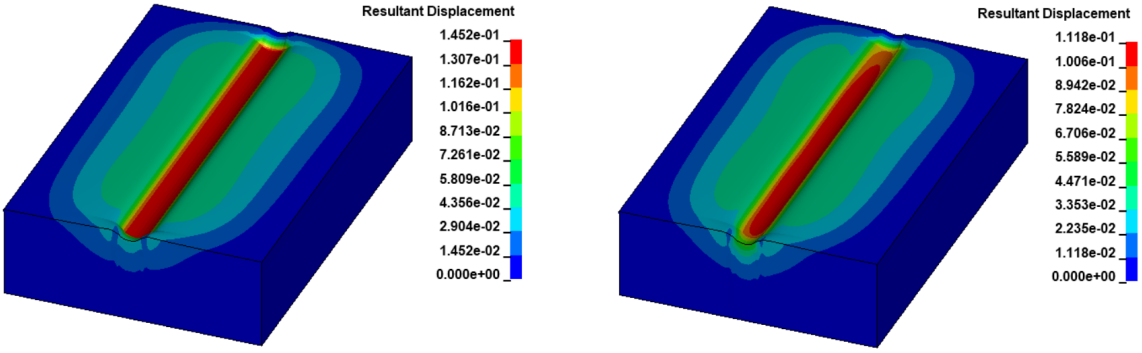

(a) At simulation time 0.3s *(b) At simulation time 0.7s*

Figure 7.15: Resultant displacement

7.9 Rigid Seabed Results

In the previous analyses, assessing the pipeline's performance was challenging, as most of the simulations resulted in permanent deformation only in the soil and the dropping object. A rigid seabed and a rigid tank have been implemented in the following simulations. It has then been possible to identify the structural response of the pipeline, without concerning the behavior of the soil and tank. In figure 7.16 the internal and kinetic energy for the three rigid seabed simulations are provided.

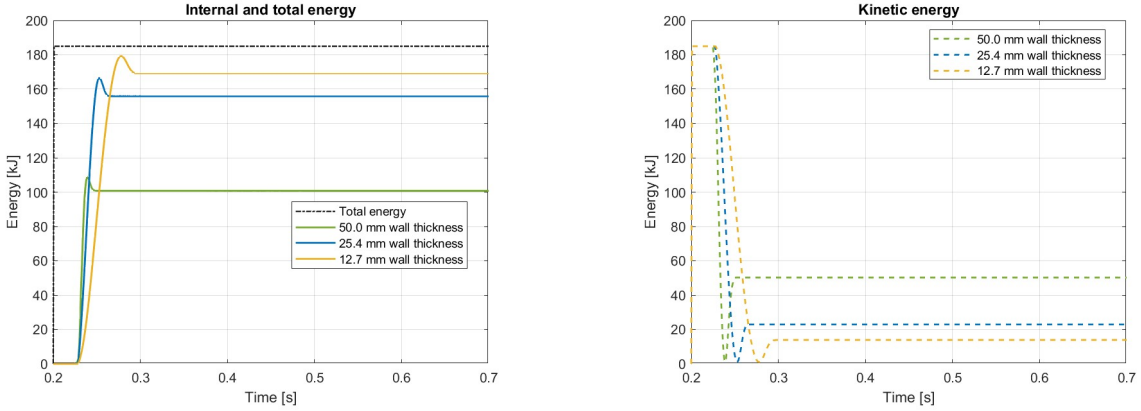

(a) Internal and total energy *(b) Kinetic energy*

Figure 7.16: Rigid tank and rigid seabed results

The deformed cross-sectional dimensions are provided in Figure 7.17. The points correspond to the coordinates of the nodes at the cross section with the highest deformation. In the figure, both the initial condition and the damaged ones are plotted for comparison.

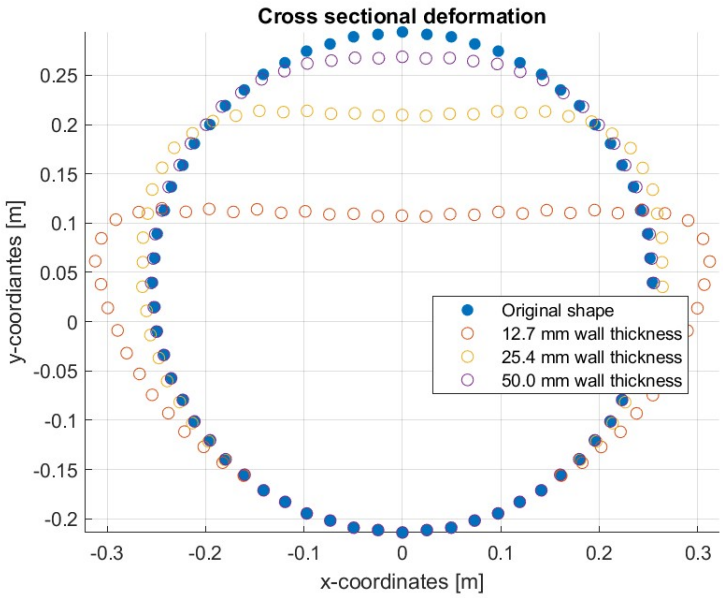

Figure 7.17: Deformed shapes

As expected, the dent depth increases with decreasing wall thickness. For a wall thickness of 50 mm, the resulting dent depth with the simulation setup used was 25.2 mm. By reducing the wall thickness to 25.4 mm a dent depth of 84.2mm was obtained. For the 12.7mm wall thickness, the resulted dent dept was 186.4mm

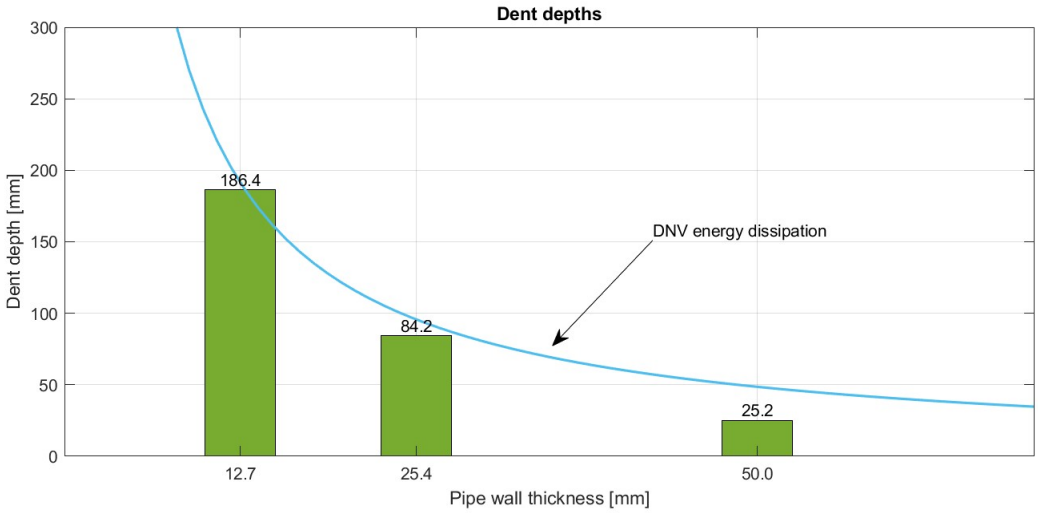

Figure 7.18: Dent depths

$$\delta = \left(\frac{E}{16}\right)\left(\frac{9}{2\pi}\right)^{0.5}\left(\frac{4\sigma_y t^2}{D}\right)^{0.5}\frac{D^{5/2}}{t^{3/2}} \tag{7.1}$$

In Figure 7.1, equation 3.8 is rearranged in terms of dent depth, δ, as a function of wall thickness, t. By substituting values for the absorbed energy, the pipeline diameter, and yield strength, the graph can be plotted and compared to the results from the simulations. As the figure shows, the obtained values through the FEA simulations align well with the approach suggested by DNV,

but there seems to be slightly more deviation when the wall thickness increases. It should be noted that the absorbed energy of the pipeline has some variation for each simulation and the average of the three is used when plotting the line. The reason of the variation can be seen in Figure 7.16, where the resulting kinetic energy and internal energy are plotted. As the total energy is constant in all cases, the reduction of internal energy for larger wall thicknesses is balanced by larger kinetic energy.

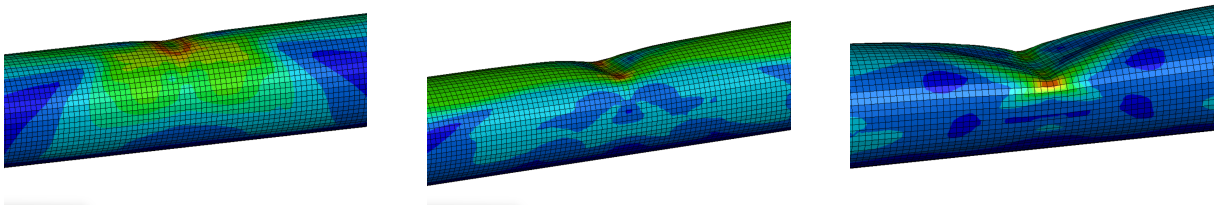

(a) 50mm wall thickness *(b) 25.4mm wall thickness* *(c) 12.7mm wall thickness*

Figure 7.19: Von Mises stress contour and deformation

The Von Mises contour plots in Figure 7.19 show the deformation and stress distribution in the pipeline for the three compared scenarios. In line with the expectations, the stresses are at their maximum in the impacted areas. In the figure, the maximum von Mises stresses range from 360 MPa for figure (a) to 520 MPa for figure (c). It can be seen that the stress concentrations occur at the boundary between the deformed and undeformed areas. Especially for the case (c), the stress concentration is high at the area between the damaged and the undamaged parts of the pipeline.

For the three wall thicknesses compared, there is a distinct relationship between the impact force and the wall thickness. Figure 7.20 shows the impact force as a function of time. As the wall thickness reduces, the time of contact increases, and the maximum impact force decreases. The maximum impact forces for the 50.0, 25.4, and 12.7mm wall thicknesses are 5.20 MN, 2.81 MN, and 1.47 MN, respectively.

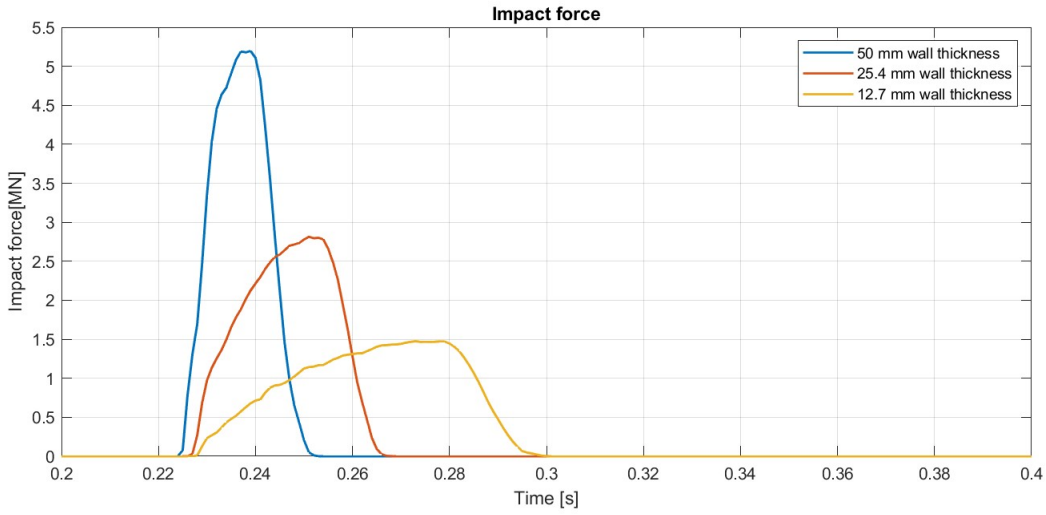

Figure 7.20: Impact force

The area enclosed by the force-time curves in Figure 7.20 equals the change in momentum of

the impact and is also known as impulse. The three cases resulted in a change in momentum of 79.6 kNs, 70.7 kNs, and 66.5 kNs for the 50.0, 25.4, and 12.7 mm thicknesses, respectively.

To see the stiffness of the pipeline, a diagram showing the contact force versus the dent depth is provided in Figure 7.21. In all cases, the curves show a linear relation between force and dent depth for small dent depths. When the load increases, the elastic regime transitions into a plastic behavior of the force-deformation curve. As in line with the expectations, the diagram shows that an increased wall thickness requires more force to produce the same dent depth.

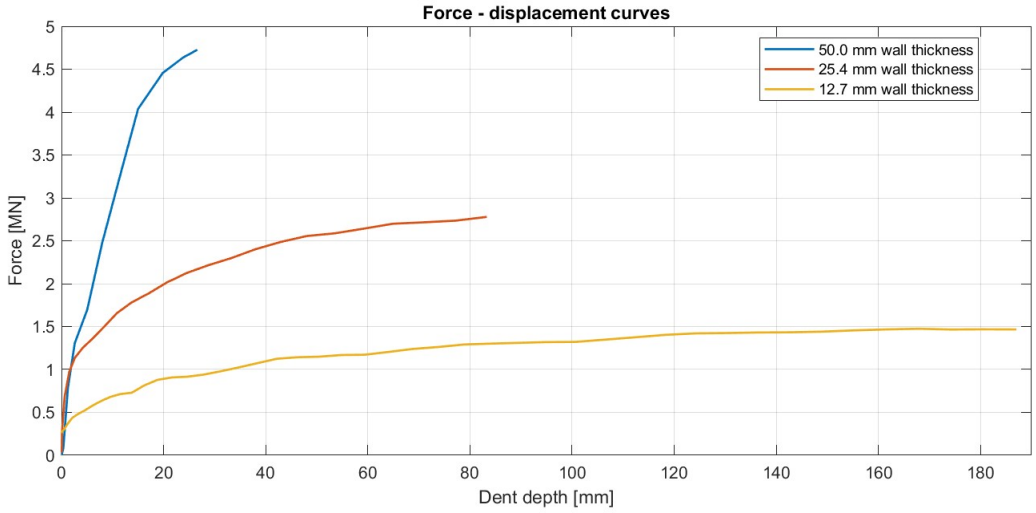

Figure 7.21: Force vs dent depth

In addition to the previously shown cross-sectional deformation, a comparison of the deformation seen from a side view is essential to be able to fully compare the structural integrity of the considered cases. Such a plot is given in Figure 7.22 and shows the deformation profile along the pipeline. From the diagram, it can be seen that the 50.0mm case, resulted in a deformed zone along the pipeline of less than 1 meter. For the 12.7mm case, the deformed zone is about 3 meters.

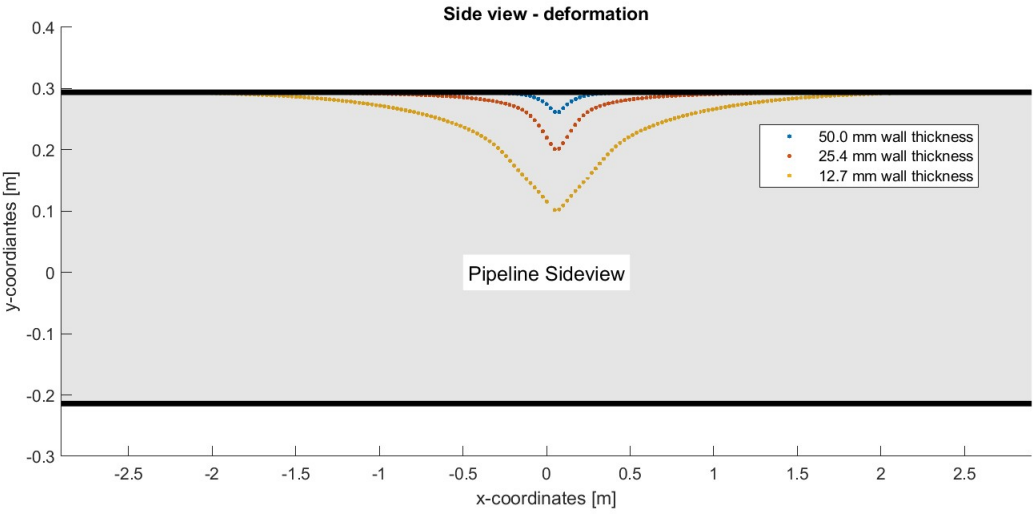

Figure 7.22: Impact force

Furthermore, the deformation profiles give information about the dent depth. As revealed in the literature review, the relation of dent depth to pipeline diameter is one of the parameters used to classify the damage of pipelines in the DNV-RP-F107. In the simulations of the 50.0 mm, 25.4 mm, and 12.7 mm wall thicknesses, the relation of dent depth to pipeline diameter measured by percentages are 4.96%, 16.6%, and 36.7%, respectively. This show that only the 50.0 mm wall thickness resulted in a damage classification minor damage (D1) as the dent depth is below 5% of pipeline diameter. The other two scenarios resulted in the damage class moderate damage (D2) or major damage (D3) depending on there is leakage or not.

The obtained deformation profiles can be compared to the empirical expression formulated by Wierzbicki and Suh, which was discussed in Section 3.3. By recalling that the formula for the affected zone (equation 3.13) depends on the maximum indentation, the pipeline diameter and the wall thickness, the theoretical values can be calculated straight forward. Below, also the observed values from the simulations are shown for comparison.

$$\xi_{50.0,model} = 261.0 \text{ mm} \qquad \xi_{25.4,model} = 669.3 \text{ mm} \qquad \xi_{12.7,model} = 1408.3 \text{ mm}$$
$$\xi_{50.0,simulation} = 284.0 \text{ mm} \qquad \xi_{25.4,simulation} = 762.8 \text{ mm} \qquad \xi_{12.7,simulation} = 1701.3 \text{ mm}$$

According to the values, the affected zone was somewhat higher than the Wierzbicki and Suh model in all three simulations. This can also be seen in Figure 7.23, where the three simulations are compared to the Wierzbicki and Suh model. Additionally, it can be observed that the profiles of the simulations experienced a greater degree of sharpness than the Wierzbicki and Suh model.

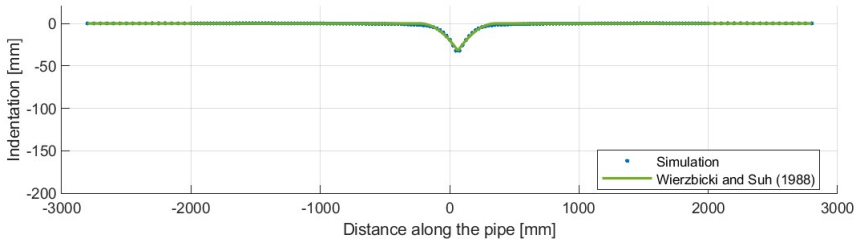

(a) 50.0 mm wall thickness

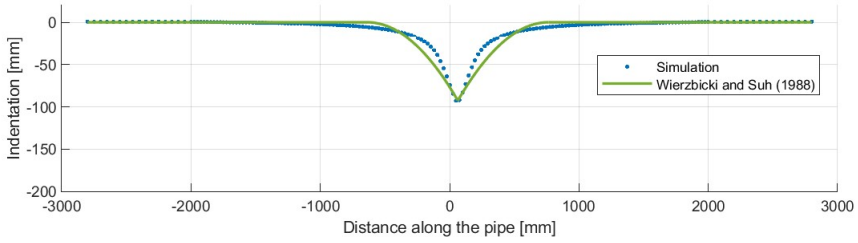

(b) 25.4 mm wall thickness

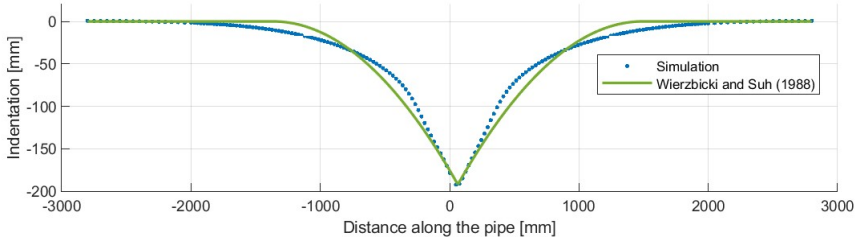

(c) 12.7 mm wall thickness

Figure 7.23: Deformation profiles

By normalizing both the Wierzbicki and Suh model and the deformation profiles from the simulations it becomes more manageable to see which of the simulation that fits best towards the empirical formulation by Wierzbicki and Suh. As the Figure 7.24 shows, the simulation with 50.0 mm matches best and there are some more deviations for the 25.4 mm and 12.7 mm.

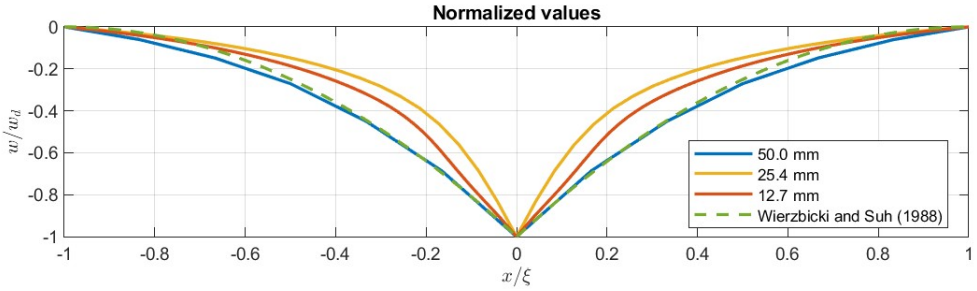

Figure 7.24: Indentation profiles

7.10 Results Overview

To summarize the results, a overview with the most important findings is provided in Table 7.2. The table contains information about the magnitude of soil displacement, dent depth, and internal energy of the pipeline. It also explains whether there was deformation of the tank and the pipeline. Similarly to the procedure performed previously in this thesis, the soil displacement shown is the maximum vertical displacement of element number 2040827 and is given in millimeters. Also the dent depth is given in millimeters and the internal energy is given in joules.

Table 7.2: Summary of the results

Sim no.	Soil	Soil displ. [mm]	Dent depth [mm]	Int. energy Pipe [J]	Tank def.	Pipe def.
1	Clay	41	-	2.3	Yes	No
2	Clay	140	-	7.9	Yes	No
3	Sand	54	-	3.3	Yes	No
4	Sand	62	-	10.6	Yes	No
5	Clay	39	-	4.1	Yes	No
6	Clay	164	-	3606.8	Yes	No
7	Sand	54	-	4.8	Yes	No
8	Sand	63	-	4214.6	Yes	No
9	Rigid	-	25.2	$101 \cdot 10^3$	Rigid	Yes
10	Rigid	-	84.2	$156 \cdot 10^3$	Rigid	Yes
11	Rigid	-	186.4	$169 \cdot 10^3$	Rigid	Yes

The last two columns indicate whether localized deformation has occurred in the pipeline and tank. In some of the cases where it is displayed "No" for pipeline deformation, it should be noted that there was a certain amount of accumulated internal energy, indicating permanent deformation in the pipeline. However, the deformation was not visible and it is therefore given "No" in the table. By comparing the internal energy with the cases of high pipeline deformation, it can be seen that the internal energy of the "No" pipeline deformation cases is small.

8 Discussion

8.1 Effect of Pipeline Wall Thickness

As mentioned previously, the dent depths according to Figure 7.18, aligned well with the rearranged DNV energy dissipation equation. The alignment to the equation was best for the 12.7 mm and 25.4 mm thicknesses, and somewhat more deviation was observed for the 50.0 mm wall thickness simulation. The reason of this is challenging to conclude on, but some of the reasons may be that the model is created in order to best fit the most commonly used wall thicknesses in pipeline engineering which is around 25 mm. When analyzing thin-walled structures, it is assumed that the stress distribution across the thickness is uniform, and this changes when the structure becomes thick-walled. Then the assumption of uniform stress distribution is invalid, indicating that the equation may only be applicable to thin-walled pipelines.

Decreasing the pipeline wall thickness will obviously decrease the pipeline's capacity towards impacts, and this has been shown through the results in the previous chapter. Quantifying the amount of capacity reduction when reducing the wall thickness of the pipeline is somewhat difficult, as all simulations were analyzed under the same loading conditions. By doing simulations with different impact loads the simulations could have resulted in near identical dent depths for different wall thicknesses which would have made it easier to estimate the actual capacity reduction. However, it is still possible to address some numbers based on the results obtained. By considering the alignment with the DNV equation for energy dissipation, the expression can be used to estimate the impact energy required for a certain dent depth to occur. By doing this and account for kinetic energy, the pipelines with 12.7 mm, 25.4 mm, and 50.0 mm wall thicknesses can withstand impact loads up estimated to around 22 kJ, 40 kJ, and 100 kJ respectively, in order to be within damage class 1.

8.1.1 Internal Energy Distribution

Figure 8.1 shows the distribution of the internal energy on the tank, soil and pipeline for the different soil types considered. This is relevant for assessing the amount of energy being dissipated in each part. The internal energy represented is the non-recoverable internal energy, which is highly associated with permanent deformations. The recoverable internal energy is related to elastic deformations and is not included to create a better picture of where permanent deformations occur. All the simulations with edge impacts (simulation 1, 3, 5, and 7) behaved quite similarly regarding the distribution of internal energy. This raises some questions when it comes to the reliability of the results, as changing the soil type did not introduce significant changes to the internal energy distribution for edge impacts. However, for the flat impacts (simulaton 2, 4, 6 and 7), the distribution is changigng somewhat more when the soil type changes. One of the possible reasons of the issue with the edge impacts could be that both soil types behave nearly identical for small loads and the difference appears when the forces increase, which was the case for when going from edge impacts to flat impacts.

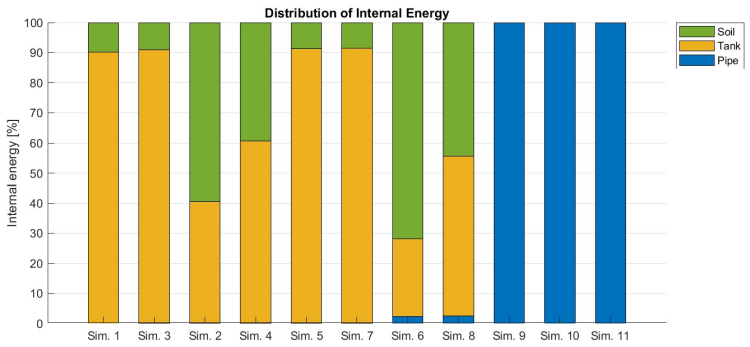

Figure 8.1: Distribution of internal energy

The three last simulations, which was with a rigid seabed and rigid tank resulted in dissipation of internal energy only in the pipeline. In these three cases, the dissipated energy was in the range of 101 kJ to 169 kJ.

8.2 Soil Behavior

One of the most challenging parts of the work throughout the thesis was related to the modeling and verification of the soil. Numerous research papers were read to find appropiate soil models and none of the soil models that were found in the research papers were employed for modeling marine soils, meaning that the soil types used in this thesis may not cover all the characteristics of marine soils. Furthermore, the large energy dissipation in the soil indicates that there is a possibility that the soil is too soft to represent average seabed conditions, but it is rather applicable for soft seabed environments.

For the simulations with soils under the pipeline, there was very small permanent pipeline deformation observed which is assumed to be because of the large energy dissipation in the tank and soil. There was more deformation and energy dissipation in the soil than what would be expected intuitively. It should also be noted that during simulations, there were some issues with large deformations in the soil. This issue was overcome by expanding the soil model so that the stress waves in the material had more elements and material to propagate through.

8.3 Simplifications and Limitations

Another topic worth discussing is that the analyzed cases are simplified problems, with elements like hydrostatic water pressure, thermal stresses and internal pressure being excluded. In a simulation of a real-world scenario this should have been included and by neglecting this, it limits the useability of the results to cases where this can be ignored. However, based upon findings in the literature review, adding internal pressure reduces the capacity, and then by neglecting this, the results from the thesis becomes more conservative.

The fact that all simulations setups were with a pipeline diameter of 508 mm and with three different pipeline wall thicknesses, the results of the pipeline behavior is only valid for these dimensions, as changing the diameter is obviously expected to change the structural response of the pipeline. However, it is assumed that the soil types considered would have responded in a close to similar way if the pipeline configurations had changed and the loading condition was the same as the contact area between the pipeline and soil does not significantly change with changing pipeline diameter.

9 Conclusion

Based on the results from the simulations and the previous chapter with discussion, some conclusions can be drawn about the pipeline's and tank's structural behavior under impact loads. The findings and insights are highlighted in this chapter and are contributions within the field of evaluating the structural response of pipelines due to impact loads.

Firstly, the structural capacity toward deformation was higher for the pipeline than the tank in both cases with wall thicknesses of 50.0 mm and 25.4 mm. In other words, the contact force between the two objects will cause the tank to dissipate more energy than the pipeline and experience more damage than the pipeline. This is particularly due to the tank's lower steel grade and the difference in geometry where the bracings, main frame, and the tank itself were more slender than the pipeline.

The rigid seabed simulations gave trustworthy results due to their alignment with the proposed method for energy dissipation of pipelines in DNV-RP-F107. The results correlated great for all the simulations, but a slightly higher deviation was observed for the 50.0 mm wall thickness. Additionally, the rigid seabed simulations also aligned well with the indentation model established by Wierzbicki and Suh, which validated their work by using three different pipeline wall thicknesses. It should also be noted that in the simulations performed in this thesis, the model was somewhat better for smaller indentations.

Moreover, the rigid simulations resulted in dent depths of 186.4 mm, 84.2 mm, and 25.2 mm. All these dent depths were obtained by an impact energy of 149,8 kJ. Based on this, it can be concluded that by neglecting energy dissipation in the soil and tank, this amount of energy will result in permanent deformation if the load is applied similar to what was done in this thesis. In other words, an impact of 149.8 kJ applied in a "knife-edge" will induce stresses beyond the range of elastic deformation and create non-recoverable deformations of 20-inches S355 pipelines with a wall thickness of 50.0 mm or less.

From the distributions of internal energy, it can be drawn some conclusions on the structural response of the pipeline and soil. For the edge impacts, the two investigated soil types seems to behave fairly similar as the changes in soil type induce a relatively small difference in the internal energy distribution. However, for flat impacts, the differences are larger, and based on the values in table 8.1, the clay is found to dissipate more energy than the natural sand.

References

[1] Dynamore Nordic AB. *Introduction to LS-DYNA*. Course content. Mar. 4, 2024. (Visited on 03/04/2024).

[2] Ansys. *LS-DYNA Keyword User's Manual*. Mar. 27, 2024. (Visited on 06/09/2024).

[3] Courtney L. Busch and Rafiqul A. Tarefder. "Evaluation of Appropriate Material Models in LS-DYNA for MM-ALE Finite Element Simulations of Small-Scale Explosive Airblast Tests on Clay Soils". In: *Indian Geotechnical Journal* 47.2 (June 1, 2017), pp. 173–186. ISSN: 2277-3347. DOI: 10.1007/s40098-016-0196-4. URL: https://doi.org/10.1007/s40098-016-0196-4 (visited on 06/02/2024).

[4] Torstein Ulland Dirdal. "Dropped object impact analysis on subsea pipelines". Accepted: 2023-07-14T15:51:29Z. Master thesis. uis, 2023. URL: https://uis.brage.unit.no/uis-xmlui/handle/11250/3078932 (visited on 06/10/2024).

[5] DYNAmore GmbH. *A review of LS-DYNA's most popular material model*. May 29, 2020. (Visited on 04/09/2024).

[6] André Haufe, Karl Schweizerhof, and Paul DuBois. "Properties & Limits: Review of Shell Element Formulations". In: *September* (2013).

[7] Fengyuan Jiang et al. "Investigation on the deformation response of submarine pipelines subjected to impact loads by dropped objects". In: *Ocean Engineering* 194 (Dec. 15, 2019), p. 106638. ISSN: 0029-8018. DOI: 10.1016/j.oceaneng.2019.106638. URL: https://www.sciencedirect.com/science/article/pii/S0029801819307589 (visited on 03/24/2024).

[8] Md. Rokan Uddin Kawsar et al. "Assessment of dropped object risk on corroded subsea pipeline". In: *Ocean Engineering* 106 (Sept. 2015), pp. 329–340. ISSN: 0029-8018. DOI: 10.1016/j.oceaneng.2015.06.056. URL: https://www.sciencedirect.com/science/article/pii/S0029801815002991 (visited on 01/15/2024).

[9] *NORSOK N-004:2022*. Standard Online. June 2022. URL: https://online.standard.no/nb/norsok-n-004-2022 (visited on 06/02/2024).

[10] Petroelumstilsynet. *Gransking etter løftehendelse med fallende gjenstand på Jotun B*. Sept. 10, 2018. (Visited on 02/25/2024).

[11] Dropped Objects Prevention Scheme. *Subsea Dropped Objects*. URL: https://www.dropsonline.org/assets/documents/DROPS-SubseaDROPS.pdf.

[12] Christoph Schmied. "Solid element formulations". In: (2022).

[13] Muhammad Tauqeer and Muk Ong. "Assessment of Impact Damage Caused by Dropped Objects on Glass Reinforced Plastic (GRP) Covers". In: June 25, 2017, V03AT02A004. DOI: 10.1115/OMAE2017-61736.

[14] Det Norske Veritas. *DNV-RP-C204 Design against accidental loads*. Mar. 4, 2024. (Visited on 03/04/2024).

[15] Det Norske Veritas. *DNV-RP-C208 Determination of structural capacity by non-linear finite element analysis methods*. Mar. 4, 2024. (Visited on 03/04/2024).

[16] Det Norske Veritas. *DNV-RP-F107 Risk Assessment of pipeline protection*. Mar. 4, 2024. (Visited on 03/04/2024).

[17] Det Norske Veritas. *DNV-ST-F101 Submarine pipeline systems*. Mar. 4, 2024. (Visited on 03/04/2024).

[18] Zhenning Wang et al. "Impact of Soil on the Penetration of Prefabricated Spherical Fragments and Its Protective Effect". In: *Applied Sciences* 13.20 (Oct. 23, 2023), p. 11567.

ISSN: 2076-3417. DOI: 10.3390/app132011567. URL: https://www.mdpi.com/2076-3417/13/20/11567 (visited on 06/02/2024).

[19] T. Wierzbicki and M. S. Suh. *Indentation of tubes under combined loading*. 1988. (Visited on 05/16/2024).

[20] A. Wright. "Tyre / soil interaction modelling within a virtual proving ground environment". In: (Jan. 2012). Accepted: 2013-05-15T19:02:46Z Publisher: Cranfield University. URL: https://dspace.lib.cranfield.ac.uk/handle/1826/7904 (visited on 06/01/2024).

[21] Gong Xiang et al. "Overview and analysis on recent research and challenges of dropped objects in offshore engineering". In: *Ocean Engineering* 281 (Aug. 1, 2023), p. 114616. ISSN: 0029-8018. DOI: 10.1016/j.oceaneng.2023.114616. URL: https://www.sciencedirect.com/science/article/pii/S0029801823010004 (visited on 01/15/2024).

[22] Kun Yang, Yanyan Sha, and Zhenhui Liu. "Dynamic Response and Damage Assessment of Subsea Pipelines Under Dropped Object Impacts". In: ASME 2023 42nd International Conference on Ocean, Offshore and Arctic Engineering. American Society of Mechanical Engineers Digital Collection, Sept. 22, 2023. DOI: 10.1115/OMAE2023-101910. URL: https://dx.doi.org/10.1115/OMAE2023-101910 (visited on 06/10/2024).

[23] M. Zeinoddini et al. "Response of submarine pipelines to impacts from dropped objects: Bed flexibility effects". In: *International Journal of Impact Engineering* 62 (Dec. 1, 2013), pp. 129–141. ISSN: 0734-743X. DOI: 10.1016/j.ijimpeng.2013.06.010. URL: https://www.sciencedirect.com/science/article/pii/S0734743X13001243 (visited on 01/17/2024).

A Appendix: Pipe Drawings

In the below figures, a 3 dimensional drawing, a side view and a cross section view of the pipeline are provided. The pipe was constructed from shell elements.

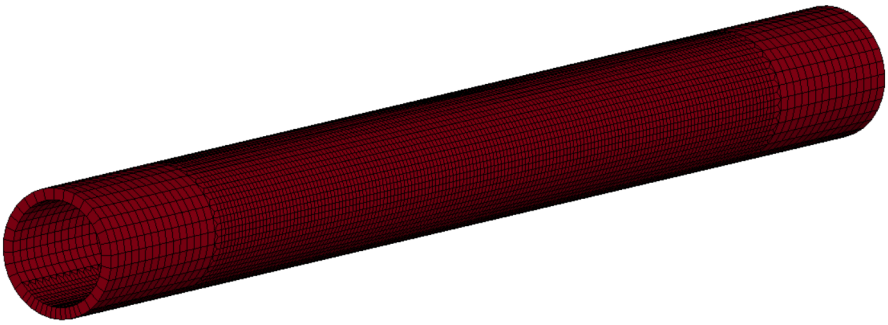

Figure A.1: 3-Dimensional Pipeline

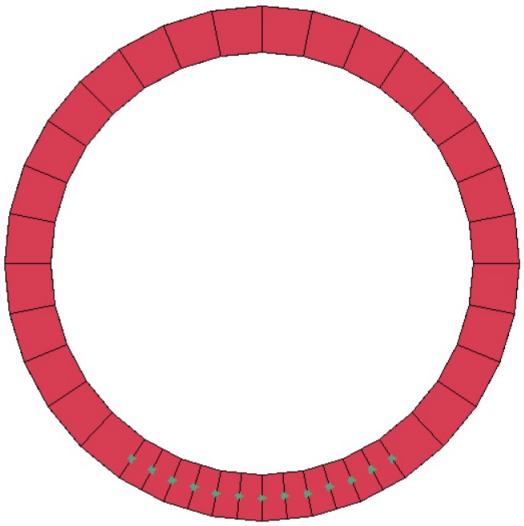

Figure A.2: Pipeline cross section

Figure A.3: Pipeline side view

B Appendix: Tank Drawings

The figures below shows a 3 dimensional drawing in addition to side view and front view of the tank. Shell elements are used for the tank.

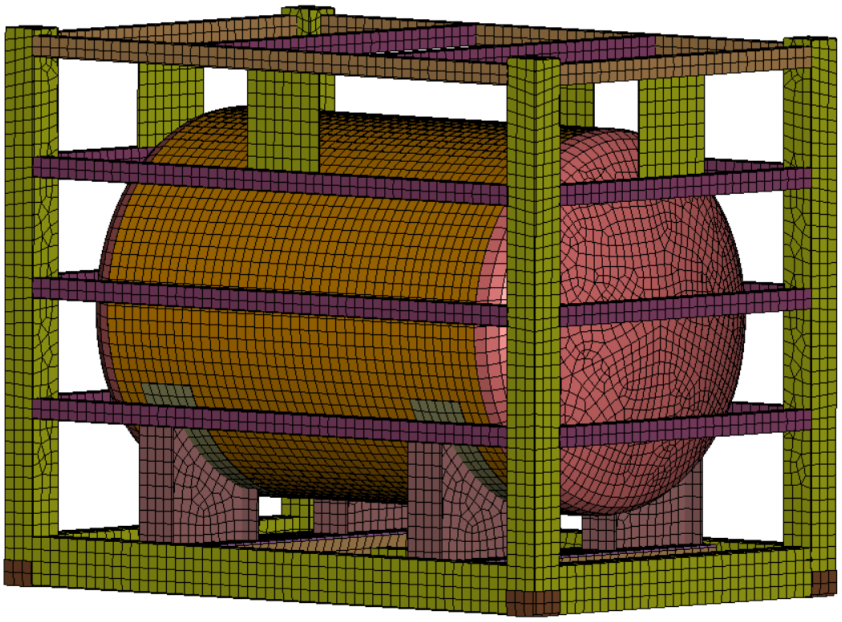

Figure B.1: 3-Dimensional tank drawing

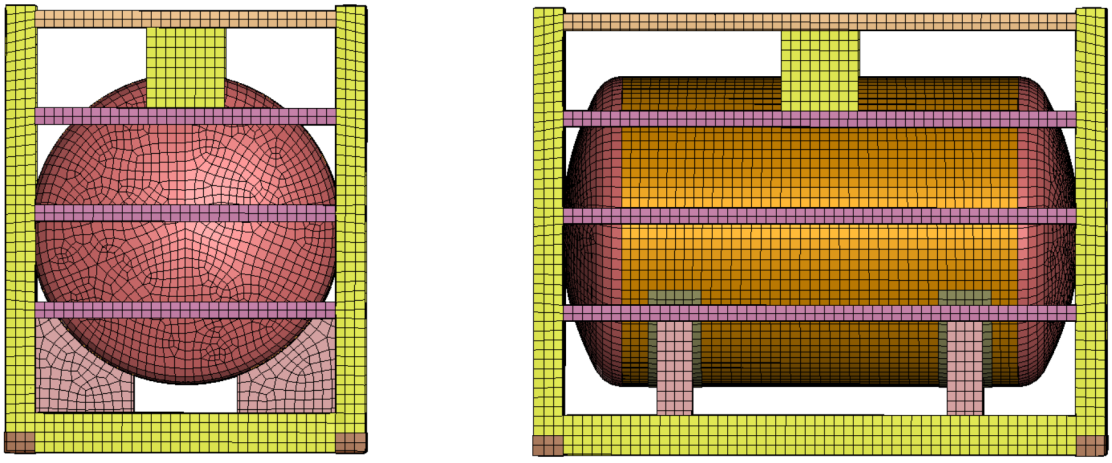

(a) Side view *(b) Front view*

Figure B.2: Tank drawings

C Appendix: Soil Drawings

The two figures below show the soil domain in a 3 dimensional view togheter with a detailed drawing of the soil mesh at the pipeline soil interaction.

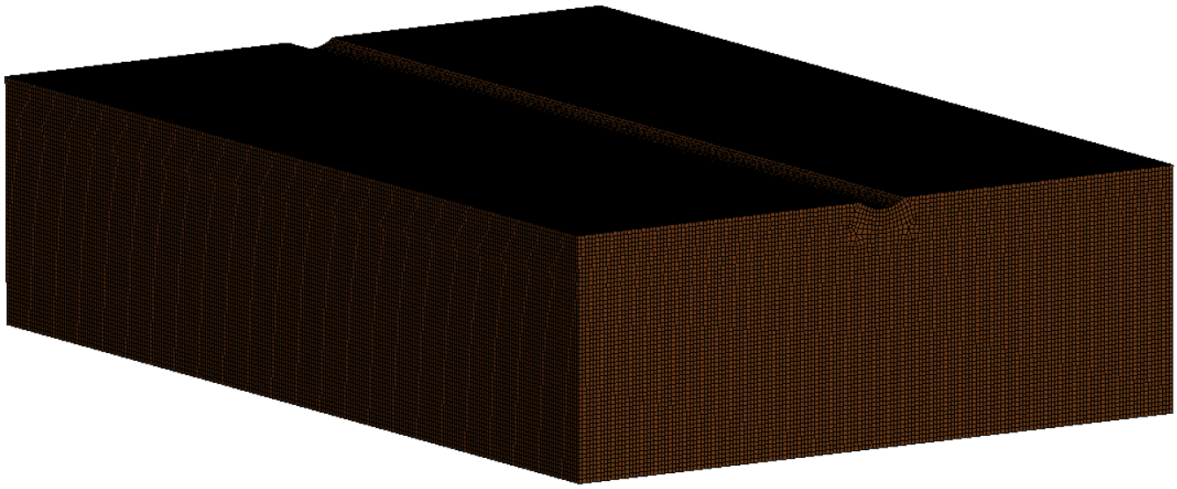

Figure C.1: Soil

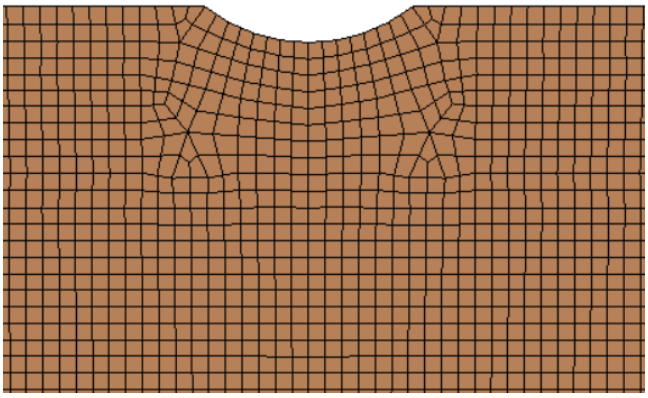

Figure C.2: Soil